NDT&E International 158 (2026) 103560

Contents lists available at ScienceDirect

NDT and E International

journal homepage: www.elsevier.com/locate/ndteint

A quantitative evaluation method for broken wires in bridge cables using 3D spatially sampled magnetic flux leakage signals

Lingsi Sun [a], Wenlong Zhang [a], Huanze Liu [a], Runyu Wang [a], Shuyu Duan [a], Lijun Jiang [b], Xinjun Wu [a,*]

[a] School of Mechanical Science & Engineering, Huazhong University of Science and Technology, Wuhan, 430074, China
[b] Liuzhou OVM Machinery Co., Ltd., Liuzhou, 545000, China

ARTICLE INFO

Keywords:
Bridge cable
Broken wire
Quantitative evaluation method
3D spatial MFL signal
L1 norm distance (L1D)

ABSTRACT

Bridge cables, which serve as critical load-bearing components in cable-supported bridges, are highly susceptible to broken wires caused by corrosion and fatigue. Accurate quantitative evaluation of this type of damage is essential to ensure structural safety. This study presents a novel quantitative evaluation method for identifying the number of broken wires by employing the magnetic flux leakage (MFL) signal in three-dimensional (3D) space. The method first acquires the 3D spatial magnetic leakage field and generates 3D arrays of MFL signals for computational analysis. It then extracts two categories of features. The first is the global feature, defined as the L1 norm distance (L1D) between the measured 3D spatial MFL signal and the defect-free reference signal. The second is the local feature, consisting of multi-scale waveform features organized as a feature array. The multi-scale waveform feature arrays are compressed using Multilinear Principal Component Analysis (MPCA) to reduce computational redundancy. The compressed feature arrays are then introduced into the Elastic Net-Constrained Regression (ENCR) model to predict defect width. The number of broken wires is ultimately calculated as the ratio of the total L1D value to the L1D value corresponding to the predicted width of a single wire. For a given broken wire width, the L1D demonstrates linear superposition with respect to the number of broken wires, with goodness-of-fit values exceeding 0.999, enabling proportional quantification. Validation through simulations and experiments on PES7-127 cables (127 wires of 7 mm diameter) confirms the method's effectiveness. The simulations achieved 100 % accuracy in counting broken wires across varying widths and distributions, while experimental results verified 100 % quantification accuracy (within a tolerance of ±1 wire) for defects involving ≤4 broken wires. This performance is obtained using a training dataset of only 30 samples. This study provides a practical and efficient approach for bridge cable assessment.

1. Introduction

Cable-supported bridge systems, including suspension bridges and cable-stayed bridges, represent the predominant structural type in long-span bridge engineering and play a critical role in enhancing transportation efficiency and mobility [1]. These bridges are typically designed for service lives exceeding 100 years, with landmark structures such as the John A. Roebling Suspension Bridge and the Manhattan Bridge operating for more than 110 years [2–4]. High-strength steel wire or strand cables constitute the primary load-bearing components of such structures. Excluding failures caused by abrupt incidents such as vehicular or vessel collisions or fire [5,6], many bridges still experience structural damage, including broken wires and corrosion, within their service life, which can ultimately result in catastrophic failure [7]. This deterioration is primarily attributed to two mechanisms: environmental degradation and evolving traffic loads. Industrial pollutants elevate atmospheric concentrations of acidic compounds, increasing the frequency of acid rain, which deteriorates metallic protective coatings on cables [5]. The compromised coatings initiate combined chemical and electrochemical corrosion processes that accelerate steel degradation and reduce mechanical performance [6]. In particular, when the High-Density Polyethylene (HDPE) protective sheath undergoes aging or mechanical damage, corrosion progression is accelerated [7]. In addition, the growing prevalence of overloaded vehicles and rising traffic density has surpassed original design specifications, leading to persistent overloading [8]. Increased vehicular speeds further amplify

* Corresponding author.
E-mail address: xinjunwu@hust.edu.cn (X. Wu).

https://doi.org/10.1016/j.ndteint.2025.103560
Received 12 August 2025; Received in revised form 11 September 2025; Accepted 22 September 2025
Available online 22 September 2025

dynamic impact loads, which, combined with environmental effects, intensify cable aging and structural deterioration [9]. Therefore, steel wires within bridge cables are increasingly prone to damage during long-term service [10]. When the extent of damage reaches critical thresholds, immediate cable replacement becomes mandatory to avoid catastrophic failure. Based on the current Technical Standard of Maintenance for City Bridges in China, cable replacement is required if the cross-sectional area of broken wires exceeds 2 % of the total cross-sectional area of the cable wires [11]. In cases of corrosion, replacement is mandated only when the cross-sectional area loss surpasses 10 %. This disparity in thresholds, 2 % for broken wires and 10 % for corrosion, highlights the more severe impact of wire breakage on the remaining service life of cables. Therefore, applying non-destructive testing (NDT) methods to detect and quantify broken wires beneath the HDPE sheath during service is essential for ensuring durability and safety [12].

At present, non-destructive testing (NDT) technologies for bridge cables primarily encompass three categories: acoustic emission (AE), ultrasonic guided wave (UGW), and magnetic flux leakage (MFL). In field applications, the effectiveness of AE techniques is restricted by the short service life of sensors and the need for advanced algorithms to filter environmental noise from AE signals generated under harsh operating conditions [13,14]. In addition, AE signal characteristics vary considerably across different bridge structures and materials, making quantitative defect assessment impractical [15]. The UGW method also faces limitations due to insufficient detection accuracy, difficulties in processing and interpreting signals caused by wave dispersion, multimodality, and modal conversion, as well as attenuation during propagation [13,16]. In contrast, MFL has gained prominence for its efficiency, quantifiable defect evaluation, and environmental adaptability, and it is extensively used in detecting damage in critical ferromagnetic components such as wire ropes, rails, and pipelines [17–19]. In recent years, numerous MFL-based bridge cable inspection systems have been developed. However, their resolutions remain limited, and only a few studies have addressed the detection of broken wires with cross-sectional losses below 2 % [20–22]. In contrast to other inspection objects, where probes can be placed directly against specimens with negligible lift-off, bridge cables pose unique challenges because of their HDPE sheaths, which range in thickness from 5 to 16 mm. These sheaths create significant lift-off distances, producing strong background magnetic fields, low signal-to-background ratios (SBR), and high sensitivity to lift-off fluctuations [23]. The research team previously developed the Radial Differential Magnetic Flux Leakage (RDMFL) method and an associated inspection system to effectively detect minor cross-sectional defects such as single broken wires. This enables reliable detection of single broken wires at any position within the cable cross-section. Experimental studies on a PES 7–127 cable specimen, composed of 127 wires each with a diameter of 7 mm, confirmed that the system achieved a detection resolution of 0.8 % of the total cross-sectional area, meeting practical engineering requirements. Based on this work, the study further investigated quantitative methods for broken wire detection in bridge cables. During operation, broken wires are most likely to occur in the surface layer of wire bundles. When the sheath is aged or damaged, the severity of corrosion decreases with increasing wire layer depth [24]. However, surface wires undergo more severe corrosion due to higher exposure to aggressive environments. Corrosion pits form localized stress concentrations, significantly reducing fatigue strength [25]. In addition, the reduction in effective load-bearing area induces stress redistribution, which accelerates crack growth under cyclic loading. This process intensifies the deterioration of mechanical properties in surface wires affected by severe corrosion, resulting in initial wire breakage in these locations. Therefore, this study focuses on the quantitative evaluation of broken wires in the surface layer.

The accurate quantification of broken wires is critical for evaluating the service life of cables, which continues to attract significant scholarly attention. Jiang employed a circumferentially distributed 12-path sensor arrangement to acquire multiple magnetic characteristic indicators and integrated them with a backpropagation (BP) neural network to achieve a quantitative evaluation of local cross-sectional loss rates in cables [10]. Ding utilized the random forest algorithm to realize the quantitative identification of the number of broken wires and cross-sectional area loss by extracting time-domain characteristics from MFL signals [20]. Liu proposed a method that extracted ten key features from MFL signals and used 1D convolutional neural networks (CNNs) for wire rope defect recognition, integrating signal preprocessing and feature engineering [26]. Although numerous quantitative methods have been proposed for cable broken wires, they predominantly rely on time-frequency domain features extracted from 2D MFL signals combined with machine learning techniques for quantification. However, these methods heavily depend on extensive prior knowledge [27]. This process is time-consuming because the characteristic parameters of MFL signals from broken wires depend not only on the number of broken wires but also on their distribution and width [12]. The construction of a database requires extensive parameter variations through experiments or simulations, particularly for cables with many steel wires, which makes the process inefficient.

This study proposes a quantitative evaluation method for broken wires in bridge cables based on 3D spatially sampled MFL signals. The method first acquires 3D leakage magnetic fields and generates MFL signals as 3D arrays. From these 3D spatial MFL signals, local features represented as multi-scale waveform feature arrays are extracted to predict broken wire widths. The method then calculates the count of broken wires under the predicted width using the linear superposition property of the L1 norm distance (L1D), a global signal feature with respect to the number of broken wires. L1D variations are primarily influenced by the width and number of broken wires while being minimally affected by their distributions. This enables the method, trained on small datasets, to achieve accurate quantification across different distributions without requiring extensive data on distribution variations. Such a design simplifies prior knowledge dataset construction and improves efficiency by reducing the time and effort required for large-scale data collection and model training. The rest of the paper is organized as follows: Section II presents the quantitative evaluation method based on 3D spatial MFL signals. Section III establishes a 3D finite element model (FEM) of MFL to determine the optimal dimension sizes of MFL signals and feature arrays used for quantification. Section IV validates the method's performance for broken wire defects with varying widths and distributions using simulation data, followed by experimental validation on a fabricated cable specimen containing multiple broken wire defects. Section V summarizes the conclusions and outlines directions for future work.

2. Method

2.1. Quantitative evaluation method for broken wires based on 3D spatial MFL signals

Fig. 1 presents the framework of the proposed quantitative evaluation method for broken wires in bridge cables using 3D spatially sampled MFL signals. This method involves four sequential steps: acquisition of 3D spatial MFL signals, extraction of features, prediction of broken wire width, and prediction of broken wire quantity. In the first step, the 3D spatial magnetic leakage field is acquired through an axial scanning strategy, where scanning is performed on a sampling plane containing multiple circumferential sampling points. This procedure generates 3D arrays of MFL signals. In the second step, two types of features are extracted. The global feature, defined as the L1 norm distance (L1D), is applied to predict the number of broken wires, while the local features, defined as multi-scale waveform features and represented as a feature array, are utilized to predict the width of broken wires. In the third step, the multi-scale waveform feature arrays undergo feature compression through Multilinear Principal Component Analysis (MPCA) to reduce

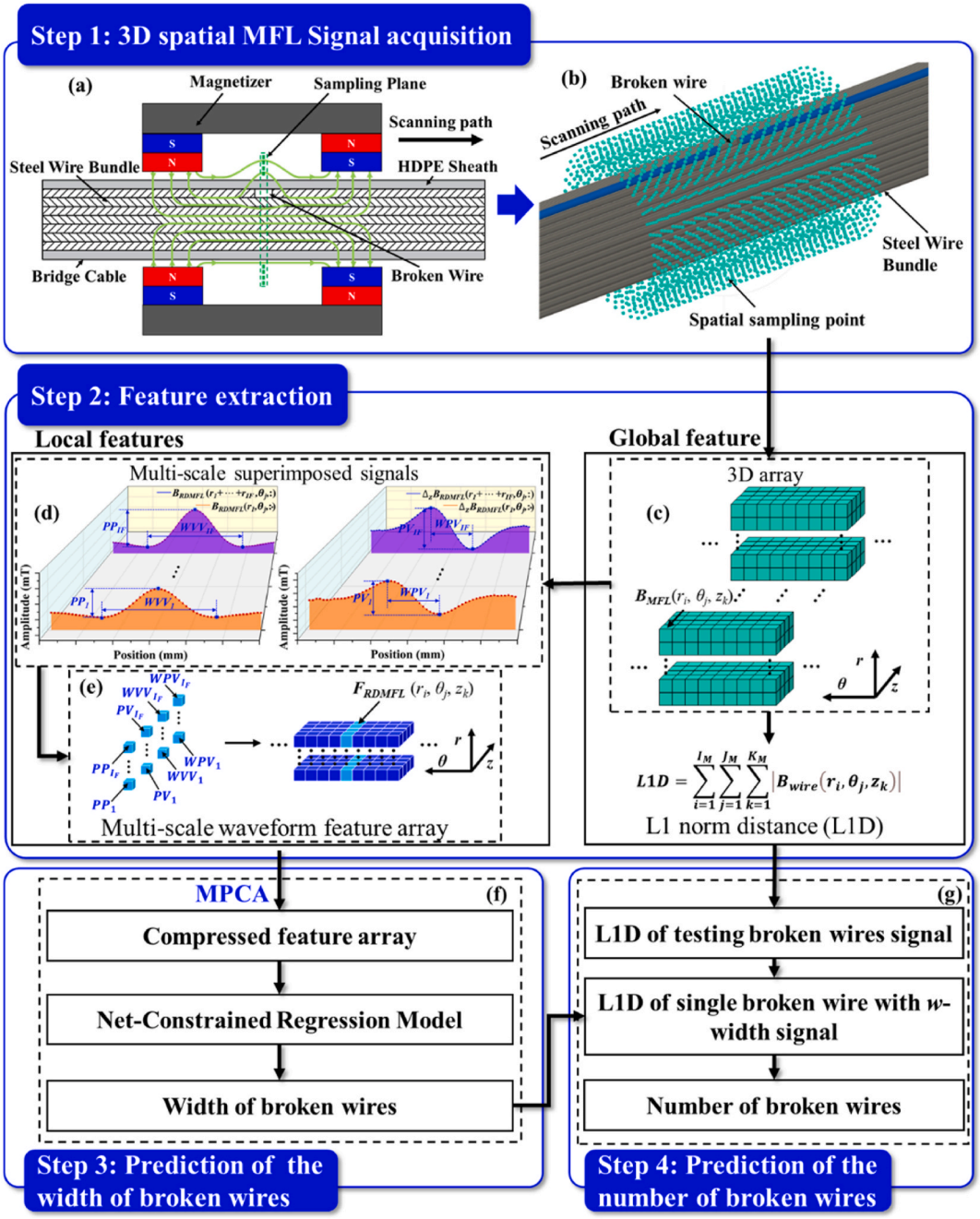

Fig. 1. Architecture of the proposed method. (a) The principle of MFL testing for broken wires in cables. (b) Schematic diagram of the spatial distribution of sampling points. (c) 3D spatial MFL signal. (d) The waveform features extracted from fibers. (e) Feature array and the elements. (f) Flowchart for the prediction of the width of broken wires. (g) Flowchart for the prediction of the number of broken wires.

computational redundancy. The compressed feature arrays are used as input for the Elastic Net-Constrained Regression (ENCR) model to predict defect width. In the fourth step, the linear superposition property of the L1D parameter at the predicted broken wire width is utilized to estimate the number of broken wires. This is achieved by dividing the total L1D ($L1D_{Total}$) of the defect by the L1D corresponding to a single broken wire ($L1D_{Single}$) of the same width. Further details of these steps are provided in the following subsections.

2.2. Step 1: 3D spatial MFL signal acquisition

The principle of MFL testing for bridge cables is shown in Fig. 1 (a). The steel wire bundle within the bridge cable is locally magnetized to saturation by a magnetizer. When a wire break occurs, magnetic flux lines leak from the magnetized cable, and the resulting leakage magnetic field diffuses into the surrounding space. A sampling plane with multiple circumferential sampling points is employed during axial scanning to capture the leakage magnetic field in 3D space. As the sampling plane moves along the cable axis, all sampling points simultaneously record MFL signals at uniform intervals. Each sampling point, however, measures only the axial component of the MFL signals. This acquisition process yields the MFL signal $B_{MFL}(r_i, \theta_j, z_k)$ at any sampling point $P(r_i, \theta_j, z_k)$, as illustrated in Fig. 1 (b), enabling the representation of the complete spatial distribution of MFL signals. Because the collected signals correspond to fixed spatial positions, the acquired MFL signals in 3D space can be naturally represented as a 3D array.

2.3. Step 2: feature extraction

The schematic diagram illustrating the 3D array representation of the 3D spatial MFL signal is shown in Fig. 1 (c). The array has dimension sizes I_M, J_M and K_M corresponding to the radial, circumferential and axial directions, respectively, with indices r_i ($i = 1, \ldots, I_M$), θ_j ($j = 1, \ldots, J_M$) and z_k ($k = 1, \ldots, K_M$). Therefore, the MFL detection signal at an arbitrary sampling point $P(r_i, \theta_j, z_k)$ can be expressed as $B_{MFL}(r_i, \theta_j, z_k)$. The measured MFL signal B_{MFL} is mainly composed of the magnetic field signal $B_{background}$ generated by the magnetizer and the magnetic field signal B_{wire} generated by the broken wire [23]. Thus, the measured MFL signal B_{MFL} at any sampling point can be represented by Eq. (1).

$$B_{MFL}(r_i, \theta_j, z_k) = B_{background}(r_i, \theta_j, z_k) + B_{wire}(r_i, \theta_j, z_k) \tag{1}$$

When no defects are present in the cable, the amplitude of the signals B_{MFL} from all sampling points fluctuates slightly within a narrow range around the background field $B_{background}$, with minor fluctuations attributable to sensor vibration and environmental interference. The occurrence of broken wires produces B_{wire}, which causes a significant deviation of the detection signal B_{MFL} from the background signal $B_{background}$. This deviation is manifested not only as amplitude anomalies at individual sampling points but also as variations across multiple points in 3D space. Therefore, the quantitative assessment of broken wires using both global and local features derived from 3D spatial MFL signals forms the technical foundation of the proposed methodology. The extraction procedures for these features are comprehensively described in this section.

2.3.1. Global feature

The L1 norm distance (L1D) is adopted to measure the deviation between the 3D arrays by considering their complex spatial relationships and structure [28]. Compared to other norm distances, L1D demonstrates robust performance against noise and outliers while maintaining computational efficiency suitable for real-time inspection scenarios [29]. The L1D for the MFL signal in this study is mathematically defined as follows:

$$L1D = \sum_{i=1}^{I_M}\sum_{j=1}^{J_M}\sum_{k=1}^{K_M}\left|B_{MFL}(r_i, \theta_j, z_k) - B_{background}(r_i, \theta_j, z_k)\right| = \sum_{i=1}^{I_M}\sum_{j=1}^{J_M} \times \sum_{k=1}^{K_M}\left|B_{wire}(r_i, \theta_j, z_k)\right| \tag{2}$$

L1D is obtained by computing the summation of absolute MFL signal amplitudes across all spatial sampling points. This parameter functions as a global feature for defect quantification. Accordingly, this study employs the relationship between the number of broken wires and the L1D of MFL signals from a high-dimensional data processing perspective to quantify wire breaks. Specifically, the number of broken wires influences B_{wire}, which in turn modifies L1D. Based on the classical point magnetic charge model for a single broken wire, under constant magnetization conditions, the magnetic field signal B_{wire} at a spatial sampling point depends on two factors: the relative position between the sensor and the broken wire, and the width of the broken wire [23,30].

Due to the global aggregation of MFL signals over circumferentially uniform sampling points, there are constantly sampling points located directly above any single surface broken wire. When the steel wire bundle is approximated as a cylinder, the spatial relationship between a broken wire at any angular position and its corresponding overhead sampling points remains invariant. Therefore, the L1D value for a single broken wire is determined only by the defect width. In addition, each broken wire can be regarded as an independent magnetic source. Based on the principle of magnetic field superposition, the leakage magnetic field in space generated by multiple broken wires is equivalent to the superposition of leakage fields from individual broken wires. L1D thus exhibits a superposition property as well. Since the sampling range fully covers the broken wire region, this superposition property is not affected by the distribution of broken wires. This relationship can be expressed as follows:

$$L1D_{Total}(Num, w) = Num^{*}L1D_{Single}(1, w) \tag{3}$$

where $L1D_{Total}(Num, w)$ is the L1D value for Num broken wires of width w, and $L1D_{Single}(1, w)$ is the L1D value for a single broken wire of width w. The core objective of this study is to quantify the number of broken wires, with the width of broken wires serving as a critical intermediate variable in this process. Accurate quantification of broken wire width is essential to ensure the reliability of the results.

2.3.2. Local features

This study proposes an innovative approach to predict broken wire width by extracting multi-scale waveform features from MFL signals. This section describes the extraction process in detail. Previous research utilized the spatial variation characteristics of MFL signals to perform radial difference and superposition processing, which generated RDMFL signals with high SBR [23]. A fiber represents a one-dimensional (1D) fragment of a multidimensional array obtained by fixing all indices except one [31]. For continuous axial scanning along the cable, fiber extraction of B_{MFL} produces continuous 1D MFL signals for a fixed sampling point $P(r_i, \theta_j)$ on the sampling plane, enabling processing and feature extraction from each axial MFL signal [32]. Fig. 2 (a) illustrates the fibers $B_{MFL}(r_i, \theta_j, :)$ of the 3D spatial MFL signal.

The fiber $B_{RDMFL}(r_i, \theta_j, :)$ is generated by implementing a differential operator on the fibers $B_{MFL}(r_i, \theta_j, :)$ to $B_{MFL}(r_{i+1}, \theta_j, :)$ at each θ_j, as illustrated in Fig. 2 (b), as defined by Eq. (4). Thus, the dimension sizes of the B_{RDMFL} array are $(I_M - 1)$, J_M and K_M.

$$B_{RDMFL}(r_i, \theta_j, :) = B_{MFL}(r_i, \theta_j, :) - B_{MFL}(r_{i+1}, \theta_j, :) \tag{4}$$

Feature extraction is performed on the fibers of the RDMFL signal, constructing the feature array $F_{RDMFL}(r_i, \theta_j, z_k)$ as depicted in Fig. 1 (d). Corresponding to the circumferential arrangement of sampling points, fibers at each angular position θ_j directly generate the elements through multi-scale signal superposition and local features extraction from the fibers of each RDMFL signal. In the superposition stage, the fibers $B_{RDMFL}(r_1, \theta_j, :) - B_{RDMFL}(r_{I_M-1}, \theta_j, :)$ are multi-scale superimposed. An example with $I_M = 4$ is given for illustration to clearly describe the superposition process. $B_{RDMFL}(r_1, \theta_j, :)$ and $B_{RDMFL}(r_2, \theta_j, :)$ are combined to generate $B_{RDMFL}(r_1 + r_2, \theta_j, :)$, while $B_{RDMFL}(r_1, \theta_j, :) - B_{RDMFL}(r_3, \theta_j, :)$ are aggregated into $B_{RDMFL}(r_1 + r_2 + r_3, \theta_j, :)$, to enhance signal amplitude as formalized in Eqs. (5) and (6). These superimposed signals characterize multi-scale radial variations of the magnetic leakage field. Axial differential signals $\Delta_z B_{RDMFL}(r_1, \theta_j, :)$, $\Delta_z B_{RDMFL}(r_1 + r_2, \theta_j, :)$ and $\Delta_z B_{RDMFL}(r_1 + r_2 + r_3, \theta_j, :)$ are obtained for their inherent advantages including mitigating low-frequency drifts, accentuating high-frequency variations induced by defects, and compressing waveform profiles [33]. Then, waveform features are systematically extracted from the multi-scale superimposed fibers. Specifically, Fig. 1 (e) indicates that peak-to-peak amplitudes (PP_1-PP_3) and valley-to-valley widths (WVV_1-WVV_3) are extracted from the B_{RDMFL} fibers, while peak-valley amplitudes (PV_1–PV_3) and peak-to-valley widths (WPV_1–WPV_3) are obtained from the $\Delta_z B_{RDMFL}$ fibers. Thus, PP and PV characterize amplitude features, whereas WVV and WPV describe spatial extents of signal profiles, enabling comprehensive waveform characterization. Thus, the dimension sizes of F_{RDMFL} array are I_F, J_F and 4, with $I_F = I_M - 1$. These features are stored in the elements of F_{RDMFL} as follows: PP_1-PP_3 correspond to the elements $F_{RDMFL}(r_1, \theta_j, 1)$-$F_{RDMFL}(r_3, \theta_j, 1)$, PV_1-PV_3 to $F_{RDMFL}(r_1, \theta_j, 2)$-$F_{RDMFL}(r_3, \theta_j, 2)$, WVV_1-WVV_3 to $F_{RDMFL}(r_1, \theta_j, 3)$-$F_{RDMFL}(r_3, \theta_j, 3)$, and WPV_1–WPV_3 to $F_{RDMFL}(r_1, \theta_j, 4)$-$F_{RDMFL}(r_3, \theta_j, 4)$.

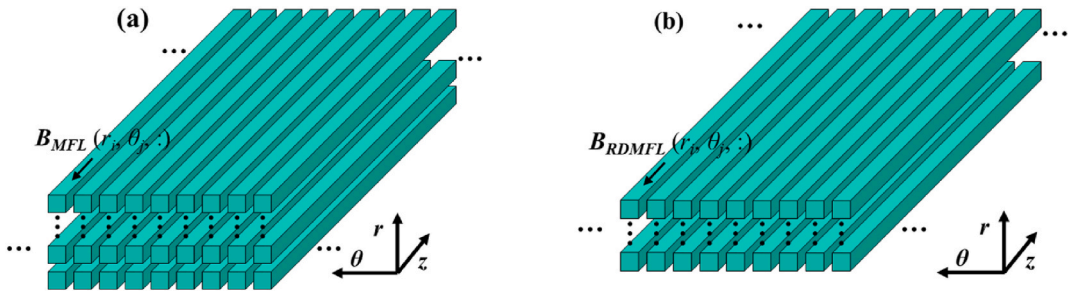

Fig. 2. (a) Fibers of MFL signal. (b) Fibers of the RDMFL signal.

$$B_{RDMFL}(r_1 + r_2, \theta_j, :), = B_{RDMFL}(r_1, \theta_j, :) + B_{RDMFL}(r_2, \theta_j, :) \tag{5}$$

$$B_{RDMFL}(r_1 + r_2 + r_3, \theta_j, :) = B_{RDMFL}(r_1, \theta_j, :) + B_{RDMFL}(r_2, \theta_j, :) + B_{RDMFL}(r_3, \theta_j, :) \tag{6}$$

2.4. Step 3: prediction of the width of broken wires

This section presents the flowchart for predicting broken wire width. Fig. 1 (f) indicates that the original feature array first undergoes feature compression through Multilinear Principal Component Analysis (MPCA) to reduce computational redundancy. MPCA derives mode-wise projection matrices $\{U^1, U^2, U^3\}$ by maximizing the variance of the projected arrays. These projections compress each dimension while preserving the 3D structure, mapping features into a space with fewer elements. The reduced features are then input into the Elastic Net-Constrained Regression (ENCR) model for predicting wire width. This step is the only stage of the method that requires training, as depicted in Fig. 3. During the training phase, an MFL signal dataset is constructed using simulation data, which covers MFL signals corresponding to various broken wires and widths. Width-related feature arrays are extracted from the simulated MFL signals to build a comprehensive feature array set. Projection matrices $\{U^1, U^2, U^3\}$ and the compressed feature array set are obtained by applying MPCA, which are utilized to train the ENCR model. In the testing phase, for target defect signals, the same MPCA compression procedure is applied using the pre-obtained projection matrices $\{U^1, U^2, U^3\}$. The compressed feature arrays are then provided as input to the trained ENCR model to predict broken wire width.

2.4.1. Multilinear Principal Component Analysis

Given the large dimensionality of the feature arrays and to mitigate collinearity and redundancy, this study applies feature compression techniques. These techniques reduce each dimension size through linear projections while retaining the 3D structural integrity of the data, preserving critical features and suppressing redundancy and noise. As a result, computational complexity is significantly reduced, and model robustness is improved through noise suppression [34]. MPCA functions as an extension of Principal Component Analysis (PCA) for multidimensional data [35]. Unlike traditional PCA, which vectorizes 2D matrices, MPCA preserves the physical structure of multidimensional arrays, avoiding structural information loss caused by vectorization. The central principle of MPCA is to maximize the variance of projected multidimensional arrays across each mode by solving mode-wise projection matrices:

$$\{U^{(n)} \in R^{I_n \times P_n}, I_n \geq P_n, n = 1, 2, \cdots, N\} \tag{7}$$

using iterative methods such as alternating least squares (ALS). These map samples $\{X_m \in R^{I_1 \times I_2 \ldots \times I_N}, m = 1, 2, \cdots, M\}$ from the original multidimensional space $R^{I_1 \times I_2 \ldots \times I_N}$ to another multidimensional space $R^{P_1 \times P_2 \ldots \times P_N}$ with reduced dimension size via:

$$Y_m = X_m \times_1 U^{(1)T} \times_2 U^{(2)T} \cdots \times_N U^{(N)T} \tag{8}$$

where $\times_N$ is the n-mode product. The compressed feature arrays $\{Y_m \in R^{P_1 \times P_2 \ldots \times P_N}, m = 1, 2, \cdots, M\}$ preserve most characteristics of the original feature arrays.

2.4.2. Elastic Net-Constrained Regression

Multidimensional data regression [36] is a statistical modeling approach designed to establish mapping relationships between multidimensional input variables and response variables. Compared to traditional scalar or vector regression methods, this approach directly processes multidimensional array structures and avoids the loss of spatial and topological information caused by vectorization [37]. This study adopts a regression framework known as Elastic Net-Constrained Regression (ENCR), which incorporates Elastic Net regularization. This framework combines the strengths of L1 and L2 norms to effectively address challenges associated with high dimensionality and feature collinearity in multi-way data [38]. In addition, the ENCR model is particularly advantageous for small-sample conditions due to its dual regularization mechanism. The regression is formulated as follows:

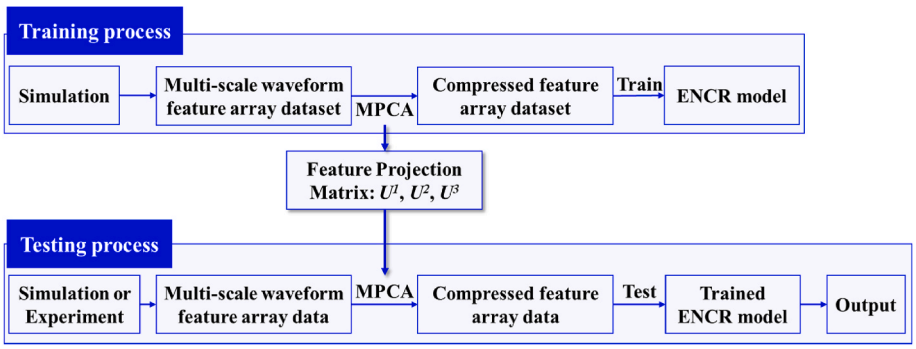

Fig. 3. The training and testing process.

$$\min_{\{W^{(n)}\}}\left\{\left\|Z-Y\times_1 W^{(1)}\times_2 W^{(2)}\cdots\times_N W^{(N)}\right\|_F^2+\lambda\left(\alpha\sum_{n=1}^{N}\|W^{(n)}\|_1+(1-\alpha)\sum_{n=1}^{N}\|W^{(n)}\|_2^2\right)\right\} \tag{9}$$

The ENCR model consists of two main components: a regression term and a penalty term. The regression term minimizes the squared Frobenius norm between the predicted values and the true broken wire widths, ensuring accurate fitting of multidimensional data. In this formulation, Y represents the input compressed feature array, while Z denotes the output scalar representing broken wire width. The expression $Y\times_1 W^{(1)}\times_2 W^{(2)}\cdots\times_N W^{(N)}$ describes the linear transformation of the input feature array Y along each mode, where $W^{(n)}$ are mode-n weight matrices. The Frobenius norm $\|\cdot\|_F^2$ measures the global discrepancy between the transformed array and the target scalar.

The penalty term employs Elastic Net regularization, which combines L1 and L2 norms to address high-dimensional modeling challenges. The L1-norm component $\left(\alpha\sum_{n=1}^{N}\|W^{(n)}\|_1\right)$ induces element-wise sparsity in the mode-n weight matrices $W^{(n)}$, performing feature selection by driving irrelevant coefficients toward zero. This reduces redundancy in high-dimensional datasets and enhances model interpretability by retaining only the most influential parameters. The L2-norm component $((1-\alpha)\sum_{n=1}^{N}\|W^{(n)}\|_2^2)$ penalizes large parameter magnitudes, thus constraining model complexity and preventing overfitting. This mechanism improves robustness by reducing sensitivity to noise and stabilizing parameter estimation. The parameter λ controls the overall regularization intensity, with larger values imposing stricter constraints on model flexibility. The parameter $\alpha\in[0,1]$ determines the balance between L1 and L2 regularization [39]. Specifically, when $\alpha=1$, the model reduces to pure L1 regularization (Lasso regression), which emphasizes sparsity, whereas when $\alpha=0$, it reduces to pure L2 regularization (Ridge regression), which emphasizes parameter stability. This dual regularization framework effectively addresses collinearity by synergistically exploiting the complementary advantages of L1 and L2 norms.

2.5. Step 4: prediction of the number of broken wires

Based on the flowchart for predicting the number of broken wires in Fig. 1 (g), the calculation is performed as follows. Once the broken wire width is determined, the number of broken wires is obtained by dividing the total L1D ($L1D_{Total}$) of the defect by the L1D of a single broken wire ($L1D_{Single}$) with the same width.

The total L1D ($L1D_{Total}$) of the measured 3D spatial MFL signal is computed. Using the predicted broken wire width from the ENCR model, the corresponding theoretical L1D value ($L1D_{Single}$) for a single broken wire of that width is obtained from precomputed calibration curves, as shown in Fig. 9, and presented in Section 3.1. The number of broken wires (Num) is then calculated by dividing $L1D_{Total}$ by $L1D_{Single}$ and rounding the result to the nearest integer, expressed as:

$$Num=round\left[\frac{L1D_{Total}(Num,w)}{L1D_{Single}(1,w)}\right] \tag{10}$$

where Num is the number of broken wires, w is the width of broken wires, $L1D_{Single}(1,w)$ is the L1D value for a single broken wire of width w, and $L1D_{Total}(Num,w)$ is the calculated L1D value for Num broken wires of width w.

3. Simulation analysis

The size parameters I_M, J_M, K_M, I_F, J_F of MFL signals and feature arrays are critical to the method, as they govern both the physical placement of the sensors and the quantification performance for broken wires. These parameters are therefore analyzed and optimized through simulation.

3.1. Determination of MFL array dimension sizes

A finite element model (FEM) for bridge cable MFL testing was established in COMSOL Multiphysics 6.0. Fig. 4 (a) indicates that the model integrates both the steel wire bundle of the bridge cable and the magnetizer. The steel wire bundle consists of 127 steel wires (7 mm diameter, 1500 mm length), while the non-ferromagnetic cable sheath is excluded from the model, with its thickness incorporated into the lift-off parameter. Fig. 4 (b) demonstrates that broken wire defects with varying numbers, widths (w), and distributions were positioned along the central axis of the cable, enabling analysis of MFL signals under different defect scenarios. The cable is magnetized using a magnetizer equipped with N52 NdFeB permanent magnets with a coercivity of 941,000 A/m and an armature. An annular refined air domain surrounding the defect regions was implemented to enhance the precision of leakage magnetic field capture. The key geometric parameters of the magnetizer and the refined air domain, including all critical dimensions (in mm), are depicted in Fig. 4 (c) and (d), respectively. The Hall element group comprises multiple sensing nodes. A previous study, considering the physical sizes of Hall sensors, determined that 4 sampling nodes arranged at 4 mm intervals represent the optimal configuration, which was validated for both SBR and signal amplitude [23]. A lift-off distance of 4 mm was adopted to eliminate frictional vibration interference during practical MFL testing. The B-H curves of the steel wire and armature materials used in this model are consistent with those adopted in earlier studies [30].

The magnetic field distribution within the cable was analyzed to validate the magnetization performance. Fig. 5 (a) indicates that the distribution of magnetic flux density Bx on the longitudinal cross-section shows that a 60 mm segment of the cable between the poles achieves a near-uniform axial magnetic flux density exceeding 1.7 T, indicating localized saturated magnetization. Fig. 5 (b) presents the magnetic field on the transverse cross-section at the central position of the cable, where the magnetic flux density varies between 1.720 and 1.727 T, confirming high uniformity. These results demonstrate that the reconfigurable magnetizer, composed of three magnetizing units arranged circumferentially at 60° intervals, can successfully achieve locally uniform and saturated magnetization of the cable. This provides the foundation for generating detectable leakage magnetic fields from broken wires, a conclusion further supported by previous experimental findings [40].

Fig. 1 (b) shows that the sampling points are arranged in a multilayer annular distribution. The MFL signal is primarily utilized to obtain the global feature L1D, with larger dimensions being more favorable. The sensor elements are arranged in multiple circumferential layers and scan along the axial direction, effectively covering both the circumferential and axial ranges of the magnetic leakage field. Therefore, the values of K_M, J_M should be increased as much as possible to ensure coverage of areas with magnetic anomalies. However, the number of sensor layers remains a key design parameter. Existing studies have shown that 4 layers represent the optimal design based on the physical size of the magnetic sensing elements, with the covered spatial sampling points ranging radially from 4 mm to 16 mm outside the cable. This study further examines the applicability of this parameter to the L1D metric.

Fig. 6 illustrates four constant-r slices (fixed radial positions) of the 3D MFL array for a single broken wire (width = 10 mm), at radial distances of 4 mm, 8 mm, 12 mm, and 16 mm from the cable surface. Red dashed lines denote axial scanning paths along the cable's axis. The circumferential angle was set to 120° with a 1° sampling interval, while in the axial direction, a 0.1 mm sampling interval was used over a 60 mm length to achieve effective circumferential signal coverage. As the number of sensor layers increases, the lift-off value gradually increases, leading to progressive attenuation of the detected signal amplitude and

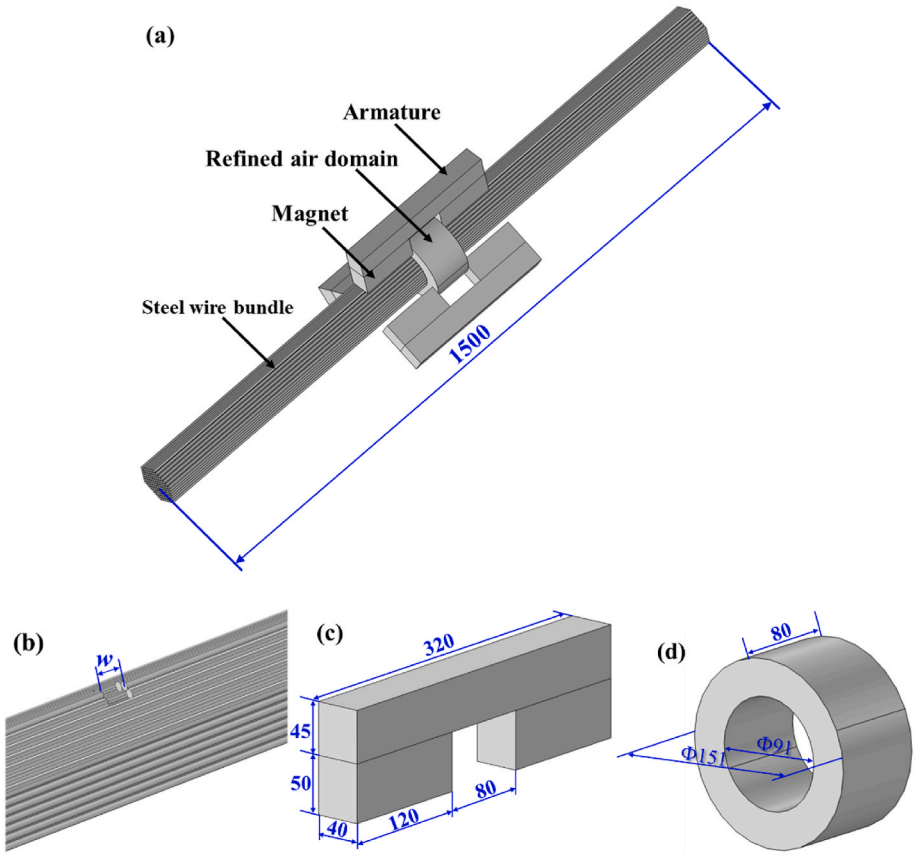

Fig. 4. (a) Finite element model of bridge cable MFL testing, (b) Broken wires. (c) Geometry size of the magnetizer. (d) Geometry size of the refined air domain.

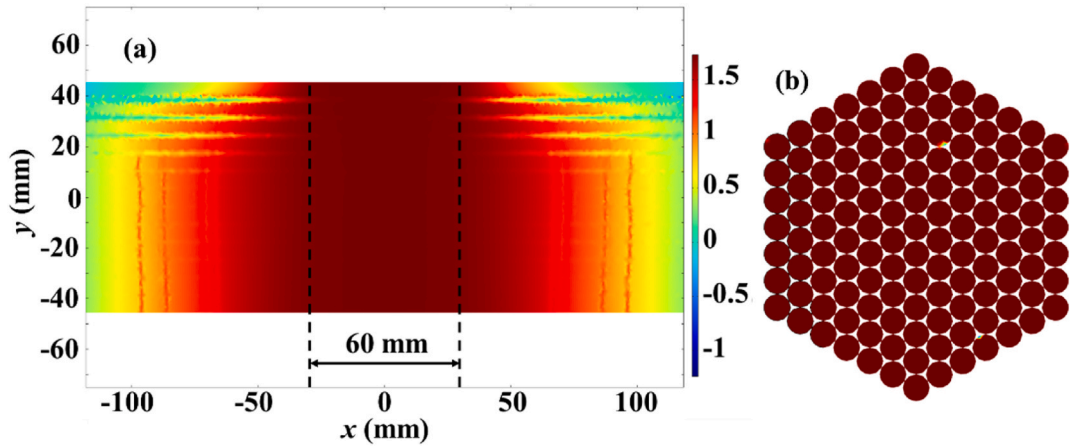

Fig. 5. (a) Distribution of magnetic flux density on the longitudinal cross-section of the cable, (b) Distribution of magnetic flux density on the transverse cross-section of the cable.

broadening of the waveform. The results demonstrate significant spatial correlations among the four array slices. The defined circumferential and axial ranges effectively cover the spatial distribution of the MFL signal; therefore, $K_M = 600$ and $J_M = 120$ are selected. With K_M and J_M fixed, the influence of variations in the radial range of the sampling point distribution outside the cable on L1D is analyzed to determine the value of I_M.

A comprehensive analysis was performed in the simulation to evaluate the effect of the radial range of sampling points on L1D. The radial range of the point cloud was extended in 2 mm increments, with the density of spatial sampling points set higher than that of the actual sensor elements to enable a more accurate assessment of distribution effects. The study examined the variation in L1D as the radial distance from the cable surface increased from 4 to 18 mm. At a radial range of 4 mm, corresponding to surface sensors in practice, the L1D value was calculated from the innermost sampling layer; at 6 mm, it was derived from the first two layers, and the process continued in this manner. When the radial range reached 18 mm, the sampling points consisted of 8 radial sampling layers. Simultaneously, the rate of contribution (ROC) of the L1D value from each newly added layer was evaluated as the radial range expanded in 2 mm increments. ROC was defined as the ratio of the L1D value of the newly added layer to the total L1D value after the addition, reflecting the influence of the new layer on the overall L1D. Fig. 7 demonstrates that the L1D value increased as the radial range of

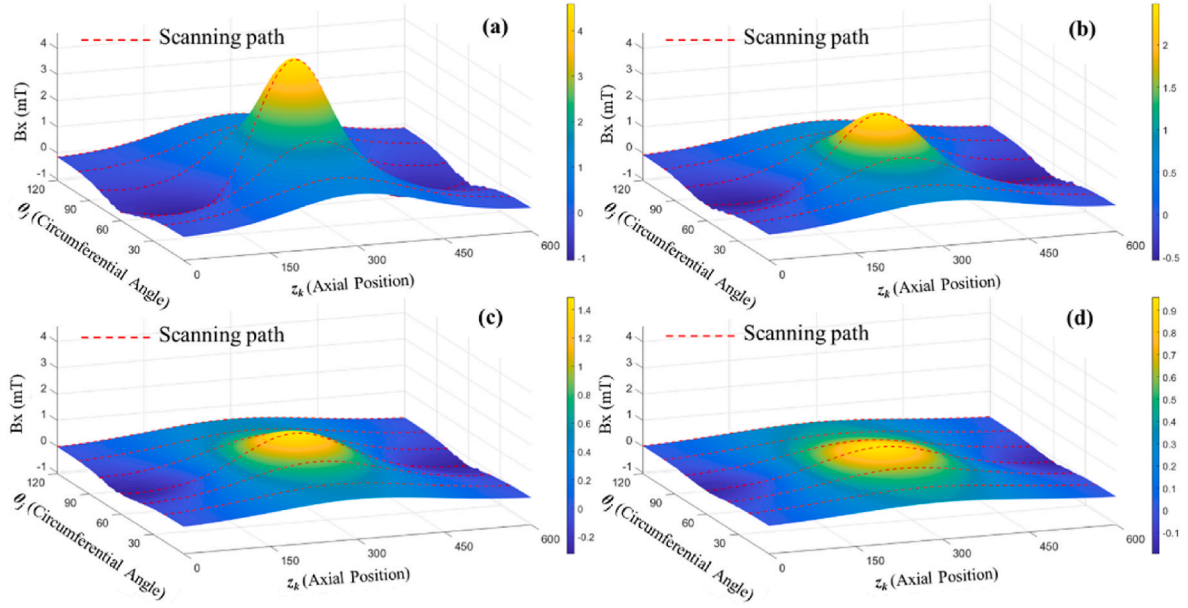

Fig. 6. Array slices of the 3D spatial MFL signal for a single broken wire at four radial sampling layers: 4, 8, 12, and 16 mm from the cable surface.

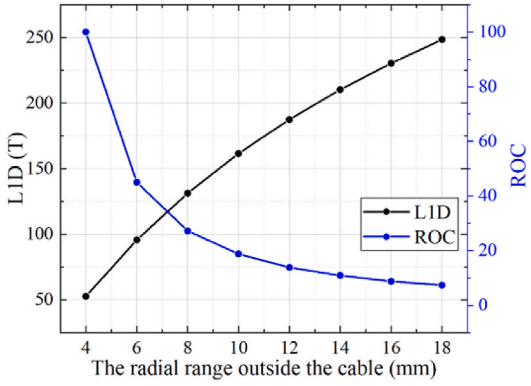

Fig. 7. Variation of the L1D value with respect to the radial range of the sampling points outside the cable.

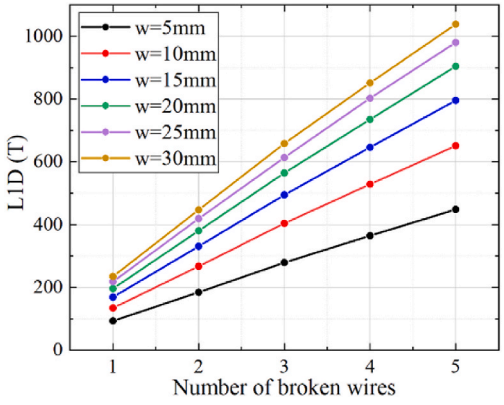

Fig. 8. L1D values of different numbers of broken wires under different widths.

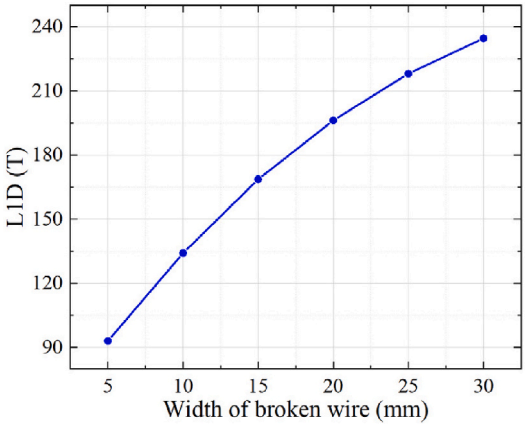

Fig. 9. L1D values of single broken wires with different widths.

sampling points outside the cable expanded, while the ROC value decreased. Specifically, when the radial range reached 16 mm, the ROC dropped to 8.7 % (below 10 %), and further increases resulted in even lower ROC values. This outcome indicates that additional sampling points beyond 16 mm contributed minimally to L1D. There is no justification for extending the radial range beyond 16 mm to optimize sensor power consumption in practical applications. The spatial region within 16 mm already provides sufficient global information to support L1D calculation, and the sampling points within this range are adequate. This range corresponds to four sensor layers, making the selection of $I_M = 4$ appropriate in this study.

Accordingly, the MFL signal array was configured with dimension sizes of $4 \times 120 \times 600$. The simulation data were further employed to analyze the variation of L1D parameters with respect to the number and width of broken wires under this configuration, verifying the applicability of L1D for predicting the number of broken wires. The simulated MFL data arrays were stored using the specified dimensional structure.

Within the FEM model, 1–5 broken wires with widths of 5, 10, 15, 20, 25, and 30 mm were modeled, and the corresponding MFL signals in 3D space were extracted and represented as 3D arrays. The L1D values of continuously distributed broken wires were calculated across varying widths, with the results presented in Fig. 8. At a fixed broken wire width of 5 mm, the L1D value increased linearly with the number of broken wires from 1 to 5. This linear trend remained consistent for wider defect widths ranging from 10 to 30 mm.

Least-squares fitting was applied to the data in Fig. 8 for six different widths to quantitatively characterize the linear dependence of L1D on

the number of broken wires (Num) for different defect widths. The equations describing the linear relationship between the number of broken wires and L1D for widths from 5 to 30 mm are provided in Eqs. (11)–(16). The coefficients of determination (R^2) all exceeded 0.999, demonstrating a strong linear correlation between these variables for the various defect widths. In addition, both the slope and the intercept of the fitted lines increased consistently with defect width, indicating that the width directly affected the coefficients of the linear relationship.

$$L1D = 89.062*Num + 6.594 \ (R^2 = 0.99938) \tag{11}$$

$$L1D = 129.527*Num + 8.443 \ (R^2 = 0.99945) \tag{12}$$

$$L1D = 156.927*Num + 16.342 \ (R^2 = 0.99956) \tag{13}$$

$$L1D = 177.082*Num + 24.765 \ (R^2 = 0.99955) \tag{14}$$

$$L1D = 190.799*Num + 34.263 \ (R^2 = 0.99946) \tag{15}$$

$$L1D = 201.176*Num + 42.343 \ (R^2 = 0.99912) \tag{16}$$

In addition, based on the simulation, the L1D values for single broken wires with widths ranging from 5 to 30 mm were extracted, with the results shown in Fig. 9. The relationship between broken wire width and L1D was also fitted, as expressed in Eq. (17). The findings indicated that L1D exhibited a nonlinear increase with broken wire width, following a quadratic relationship.

$$L1D = -0.124*w^2 + 9.971*w + 46.569 \ (R^2 = 0.99996) \tag{17}$$

The linear superposition properties of L1D for broken wires were further examined by considering the effect of broken wire width on L1D values. Specifically, using the L1D value of a single broken wire with width w as a reference, the L1D values for multiple broken wires were estimated through linear superposition of this baseline value. This relationship was expressed by the formula:

$$L1D_{Predicted}(Num, w) = Num*L1D_{Single}(1, w) \tag{18}$$

where $L1D_{Predicted}(Num, w)$ is the calculated L1D value for Num broken wires of width w. Fig. 10 exhibits that both $L1D_{Predicted}(Num, w)$ derived from the linear superposition principle and the corresponding actual values $L1D_{Total}(Num, w)$ are presented. Fig. 10 (a) demonstrates good agreement between $L1D_{Total}$ and $L1D_{Predicted}$ for 5 mm broken wires across different numbers, in accordance with equation (18). In addition, results from Fig. 10(b)–(f) indicate that as broken wire width increases, the consistency between predicted and actual L1D values decreases for varying numbers of broken wires. The relative error was calculated using the following formula to quantify this discrepancy:

$$Relative\ error(Num, w) = \frac{L1D_{Predicted}(Num, w) - L1D_{Total}(Num, w)}{L1D_{Total}(Num, w)} * 100\% \tag{19}$$

Fig. 11 reveals that the relative errors between $L1D_{Predicted}$ and $L1D_{Total}$ were evaluated. For a fixed broken wire width, the relative error increased as the number of broken wires grew. Similarly, when the number of broken wires was held constant, the relative error increased with greater defect width. The maximum error, 12.97 %, occurred at a width of 30 mm with 5 broken wires. The primary cause of these errors was that the actual wire bundle was polygonal rather than circular, as demonstrated in Fig. 4. Therefore, the relative distance between newly added broken wires on the surface and their corresponding overhead detection points was not perfectly constant. In contrast, the ideal superposition model in Eq. (18) considered only the linear summation of L1D values and disregarded the actual geometry of the wire bundle. As analyzed earlier, when the relative distance between a broken wire and the sampling points increased, the actual MFL signal values decreased, leading to a slight overestimation of $L1D_{Predicted}(Num, w)$ relative to $L1D_{Total}(Num, w)$. Despite these discrepancies, the errors remained small, confirming that the linear superposition property was valid for

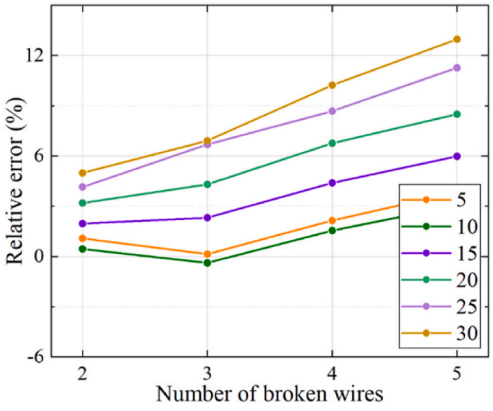

Fig. 11. Relative errors between $L1D_{Predicted}$ and $L1D_{Total}$.

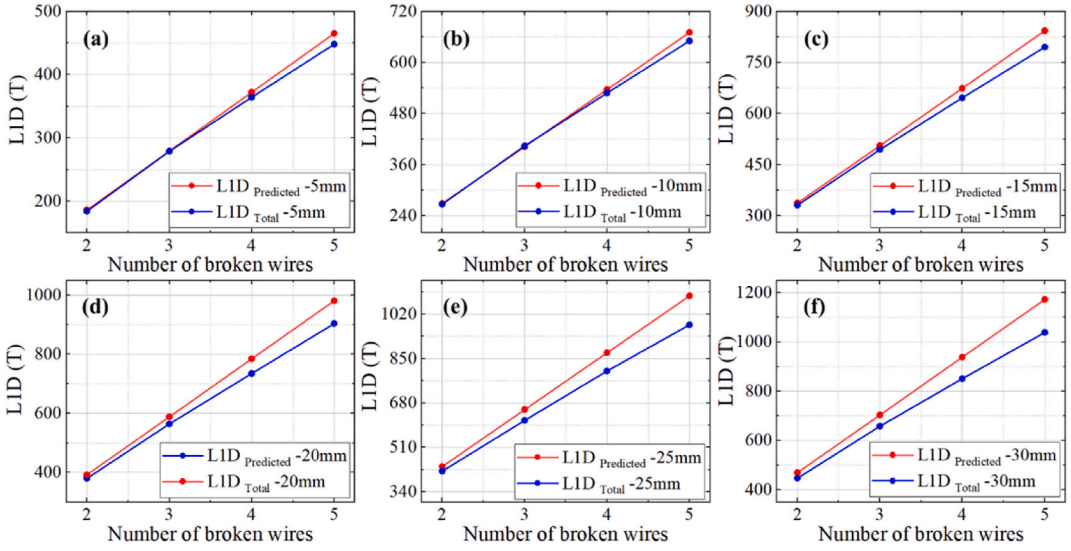

Fig. 10. $L1D_{Predicted}$ and $L1D_{Total}$ with different broken wire numbers and widths.

quantifying the number of broken wires. Therefore, once the intermediate variable of broken wire width is determined, the number of broken wires *Num* can be reliably quantified using L1D values.

3.2. Determination of the feature array dimension sizes

Then, the size parameters I_F and J_F of the feature array were determined via simulation. Because I_F is equal to $I_M - 1$ and I_M was optimized to 4 in Section 3.1, I_F was determined to be 3. The size parameter J_F of the feature array was derived by analyzing circumferential amplitude attenuation across each radial layer under varying broken wire parameters to preserve valid information while avoiding redundancy, defining an effective angular range (EAR) for feature extraction. The −6 dB threshold (50 % amplitude attenuation) was adopted to retain most of the raw signal information [41]. Initially, the attenuation of *PP* and *PV* values for broken wires of different widths and quantities was analyzed. Fig. 12 illustrates the circumferential distributions of *PP* and *PV* values for a single 10 mm wide broken wire in the simulation. Values attenuated symmetrically from the 0° center, with −6 dB defining EARs of: 30°, 32°and 32° for PP_1–PP_3; 26°, 28°, 28° for PV_1–PV_3.

Simulations were conducted for single broken wires with widths ranging from 5 to 30 mm, and the EARs of PP_1–PP_3 and PV_1–PV_3 were obtained to examine the influence of single broken wire width on the EAR, as shown in Fig. 13. Results indicated that the EARs of PP_1–PP_3 increases monotonically with width, reaching maximum values of 34°, 36°, and 38° at 30 mm. In contrast, the EAR of PV_1 remains relatively stable, fluctuating slightly within the range of 26°–27° due to simulation errors. For PV_2, the EAR increases within 5–10 mm before stabilizing at 28°. The EAR of PV_3 rises from 10 to 15 mm and then stabilizes at 30° for widths greater than 15 mm.

Simulations employed a 30 mm wide single broken wire, which corresponded to the maximum EAR observed in single-wire scenarios, to investigate the influence of the number of broken wires on EAR. Based on the Standard of Maintenance for City Bridges, cable replacement is required when broken wires exceed 2 % of the total wires. For the PES7-127 cable with 127 wires, this threshold corresponds to 3 broken wires. Simulations were conducted to obtain the EARs of PP_1–PP_3 and PV_1–PV_3 for 1 to 5 broken wires, each 30 mm wide. Fig. 14 indicates that the EARs increase monotonically with the number of broken wires, with PP_3 and PV_3 consistently exhibiting the maximum values. When the number of broken wires reaches 5, the EAR of PP_3 extends to 60°, and that of PV_3 reaches 48°. Thus, the maximum EAR for subsequent studies was determined to be 60°, meaning J_F for feature extraction was set to 60. Accordingly, the size of the constructed feature array for each defect was set to $3 \times 60 \times 4$.

The influence of broken wire width on the elements of the feature array $F_{RDMFL}(r_i, \theta_j, z_k)$ was analyzed by fixing the number of broken wires at 1 and varying the width from 5 to 30 mm. Several typical elements of the feature array were selected for analysis. With an EAR of 60°, the angular positions correspond to specific indices: −30° maps to $\theta_1 = 1$, 0° to $\theta_{30} = 30$, and 30° to $\theta_{60} = 60$. Similarly, r_1-r_3 correspond to 1–3. This study first analyzed the effect of width on $F_{RDMFL}(1, \theta_j, 1)$ to $F_{RDMFL}(3, \theta_j, 1)$, which correspond to the PP_1-PP_3 values. Fig. 15 (a) indicates that the amplitudes of PP_1 under various broken wire widths exhibit significant differences: the values of $F_{RDMFL}(1, 30, 1)$ are significantly higher than those of $F_{RDMFL}(1, 1, 1)$ and $F_{RDMFL}(1,60,1)$, with high consistency between the two side values due to symmetry. Specifically, $F_{RDMFL}(1, 30, 1)$ first rises and then reduces with increasing broken wire width, peaking at 15 mm. In contrast, $F_{RDMFL}(1, 1, 1)$ and $F_{RDMFL}(1, 60, 1)$ reach their maximum at 20 mm, differing from the peak position of $F_{RDMFL}(1, 30, 1)$. The variation trends of $F_{RDMFL}(2, \theta_j, 1)$ and $F_{RDMFL}(3, \theta_j, 1)$ shown in Fig. 15 (b) and (c) are consistent with those of $F_{RDMFL}(1, \theta_j, 1)$. However, due to signal superposition, the values of $F_{RDMFL}(2, \theta_j, 1)$ and $F_{RDMFL}(3, \theta_j, 1)$ are all higher than those of $F_{RDMFL}(1, \theta_j, 1)$.

Fig. 16 shows that $F_{RDMFL}(1, \theta_j, 2)$ to $F_{RDMFL}(3, \theta_j, 2)$ correspond to the PV_1-PV_3 values. The amplitude variation trends of these elements are similar to those of $F_{RDMFL}(1, \theta_j, 1)$ to $F_{RDMFL}(3, \theta_j, 1)$, but the widths at which their maximum values occur differ.

$F_{RDMFL}(1, \theta_j, 3)$ to $F_{RDMFL}(3, \theta_j, 3)$ correspond to the WVV_1-WVV_3 values. Fig. 17 (a)–(c) reveal that these parameters exhibit a monotonically increasing trend with increasing broken wire width. Values at $\theta_j = 1$ and 60 are overall higher than those at $\theta_j = 30$, but the variation rate at $\theta_j = 30$ is significantly greater than at the other positions.

$F_{RDMFL}(1, \theta_j, 4) - F_{RDMFL}(3, \theta_j, 4)$ correspond to the WPV_1-WPV_3 values. Fig. 18(a)–(c) exhibit that these parameters all exhibit a monotonically increasing trend with increasing broken wire width, featuring similar variation rates across different angles, while maintaining consistently higher values at $\theta_j = 1$ and 60.

These results demonstrate a strong correlation between broken wire width and feature array elements, indicating that these elements can be used for width estimation. *PP* and *PV* exhibit collinearity, while *WVV* and *WPV* also display strong correlations, indicating that their variations are positively associated with increasing broken wire width.

4. Method verification

4.1. Method verification by simulation

4.1.1. Verification of the method for broken wires with different widths

A training dataset comprising 30 samples was constructed using the 3D FEM model established in Section 3.1 and the corresponding simulation data. This dataset covered circumferentially distributed broken

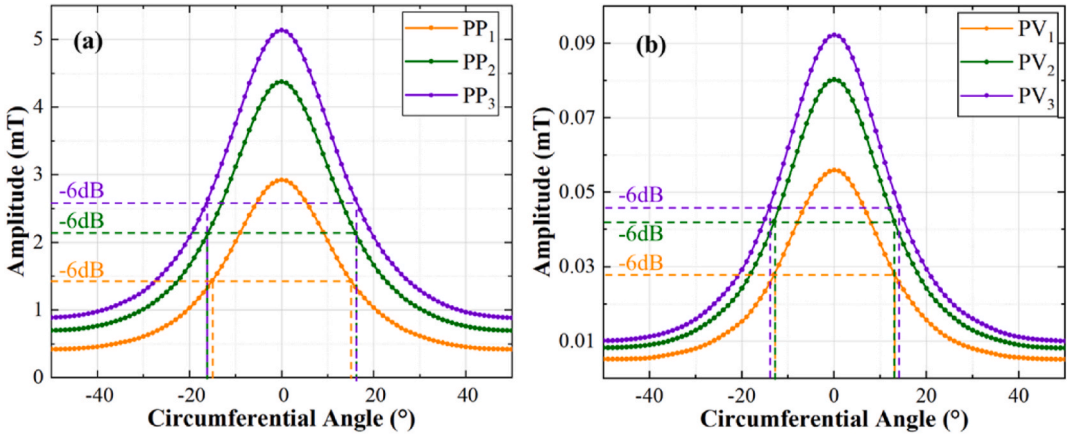

Fig. 12. (a) *PP* amplitudes measured at different circumferential angles. (b) *PV* amplitudes measured at different circumferential angles.

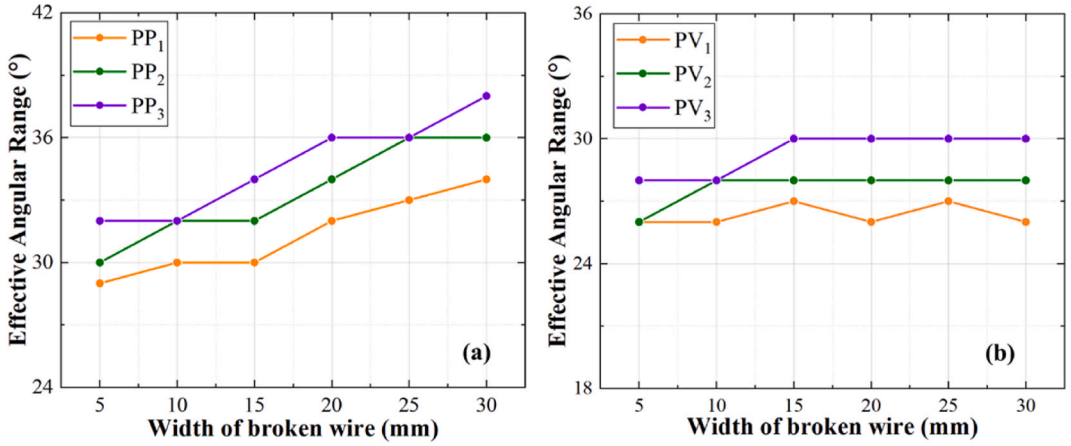

Fig. 13. (a) Effective angular range of *PP* values under different broken wire width. (b) Effective angular range of *PV* values wire under different broken wire width.

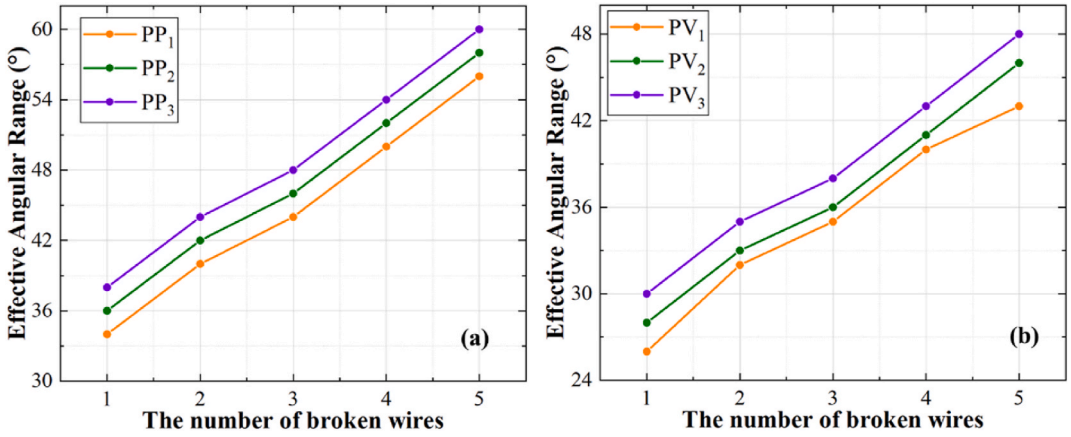

Fig. 14. (a) Effective angular range of *PP* values under different numbers of broken wires. (b) Effective angular range of *PV* values under different numbers of broken wires.

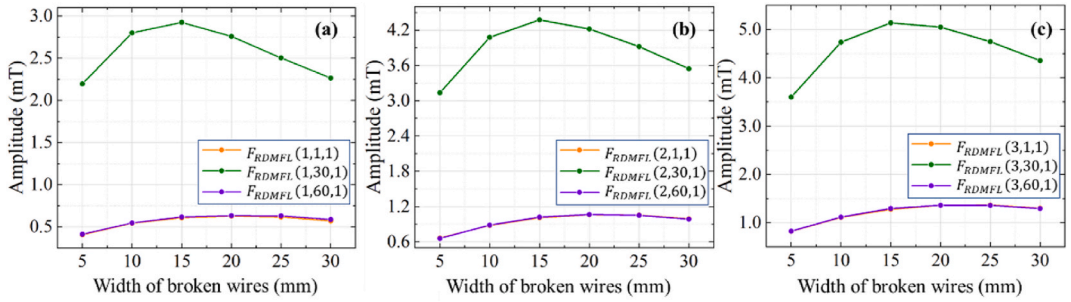

Fig. 15. Influence of the width of the broken wire on $F_{RDMFL}(1,\theta_j,1)$ to $F_{RDMFL}(3,\theta_j,1)$.

wire defects with widths ranging from 5 to 30 mm and numbers of broken wires ranging from 1 to 5, as illustrated in Fig. 19 (a)–(e). The validation set, consisting of multiple clusters of broken wire defects with quantities ranging from 2 to 5 and specific widths of 7, 12, 14, 18, 22, and 28 mm, is listed in Table 1 and was used for prediction. The bridge cable in the FEM model contained only one cluster of broken wires, and each simulation represented a single combination of broken wire width and number. The method was implemented based on the procedures outlined in Section 2.1, with parameter configurations as follows: the angular range for L1D calculation was set to 120°, the EAR for feature extraction was set to 60°, and the feature arrays (3 × 60 × 4) were constructed in accordance with Section 3.2. Feature compression was performed using MPCA with a cumulative variance ratio of 0.97 to retain most of the feature information. This configuration reduced the dimensions of the feature array from 3 × 60 × 4 to 2 × 16 × 3. The ENCR model was trained with a regularization strength of $\lambda = 2$, a mixing parameter of $\alpha = 0.8$, and a maximum iteration limit of 2000. Table 1 indicates that Defects 1# to 3# contained the same number of broken wires but differed in width, with each defect containing 3 broken wires of 7, 14, and 28 mm, respectively. The predicted widths were 7.26, 13.68, and 28.22 mm using the proposed method. The maximum relative error of defect width prediction was 3.71 %, while the minimum error was only 0.78 %. After the broken wire widths were determined, $L1D_{Single}$ values for these widths were computed using Eq. (17). The

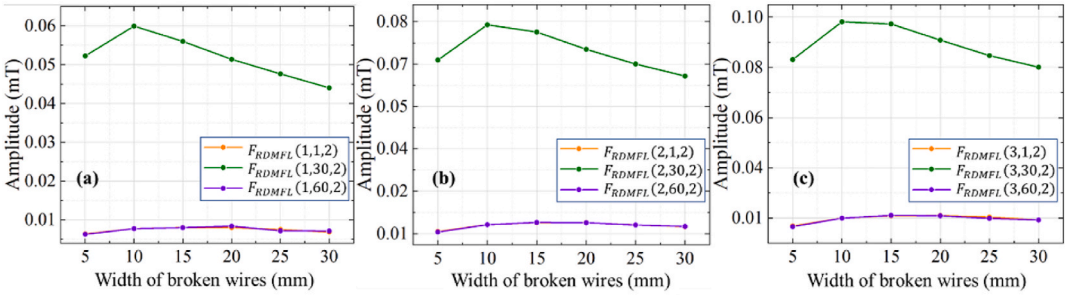

Fig. 16. Influence of the width of the broken wire on $F_{RDMFL}(1,\theta_j,2)$ to $F_{RDMFL}(3,\theta_j,2)$.

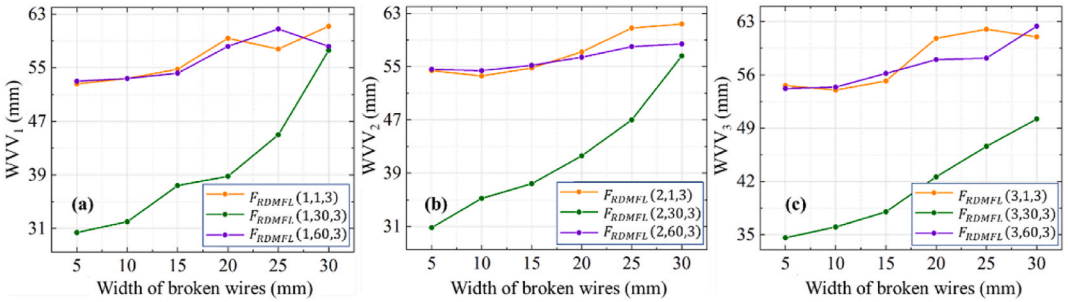

Fig. 17. Influence of the width of the broken wire on $F_{RDMFL}(1,\theta_j,3)$ to $F_{RDMFL}(3,\theta_j,3)$.

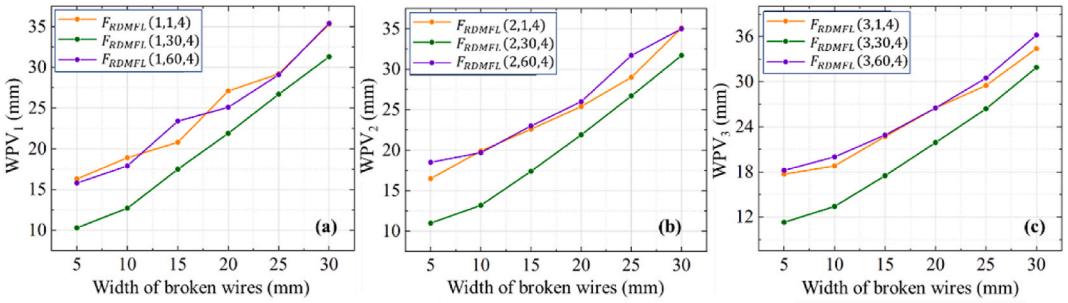

Fig. 18. Influence of the width of the broken wire on the $F_{RDMFL}(1,\theta_j,4)$ to $F_{RDMFL}(3,\theta_j,4)$.

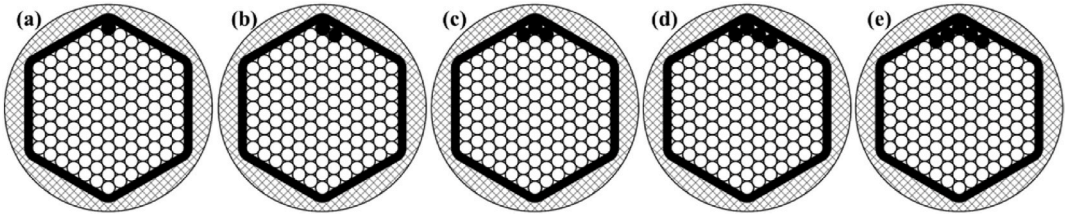

Fig. 19. Schematic of continuously distributed broken wires along the circumference within the cross-section.

corresponding $L1D_{Total}$ values of these defects were calculated directly, and all values are summarized in Table 1. The number of broken wires was determined by dividing $L1D_{Total}$ by $L1D_{Single}$, and the calculated values are presented in the table, marked with red numbers in parentheses. Rounding these values to the nearest integer yielded the final predicted numbers of broken wires, which matched the preset values.

In addition, Defects 4# to 6# exhibited variations in both the number of broken wires and their widths, consisting of 2, 4, and 5 broken wires with corresponding widths of 22, 12, and 18 mm, respectively. The corresponding signals were processed using the same procedure. The predicted widths of these defects were 21.92, 11.48, and 18.46 mm, yielding a maximum relative error of −4.33 % and a minimum of −0.36 %. These findings demonstrate that the proposed method provides high accuracy in predicting defect widths. In addition, the predicted numbers of broken wires matched the preset values in all cases. Therefore, the results confirm that the proposed method enables precise prediction of both the number of broken wires and their corresponding widths.

4.1.2. Verification of the method for broken wires with different distributions

Since the distribution of broken wires within the cross-section influences the leakage magnetic field distribution and affects the MFL signal, the effect of different sectional distributions of broken wires on the proposed method was systematically analyzed [42]. Simulations

Table 1
Quantification results of broken wires with different widths.

Defects	1#	2#	3#	4#	5#	6#
The preset broken wire numbers	3	3	3	2	4	5
The preset broken wire widths (mm)	7	14	28	22	12	18
The predicted broken wire widths (mm)	7.26	13.68	28.22	21.92	11.48	18.46
$L1D_{Single}$ (mT)	112.59	160.12	229.31	205.30	145.11	188.37
$L1D_{Total}$ (mT)	334.32	477.70	643.07	398.02	579.28	864.26
The predicted broken wire numbers	3 (2.97)	3 (2.98)	3 (2.80)	2 (1.94)	4 (3.99)	5 (4.59)

Table 2
Quantification results of broken wires with different distributions.

Defects	1#	2#	3#	4#	5#	6#
The preset broken wire numbers	2	2	2	3	3	3
Distributions	1	2	3	1	2	3
The predicted broken wire widths (mm)	9.69	10.41	11.47	10.17	10.73	9.13
$L1D_{Single}$ (mT)	131.93	137.34	145.04	135.55	139.70	127.62
$L1D_{Total}$ (mT)	246.72	236.13	229.84	368.49	352.21	342.05
The predicted broken wire numbers	2 (1.87)	2 (1.72)	2 (1.58)	3 (2.72)	3 (2.52)	3 (2.68)

Table 3
Quantification results of broken wires with different distributions.

Defects	7#	8#	9#	10#	11#	12#
The preset broken wire numbers	4	4	4	5	5	5
Distributions	1	2	3	1	2	3
The predicted broken wire widths (mm)	10.36	10.37	10.87	11.02	9.92	10.59
$L1D_{Single}$ (mT)	136.97	137.04	140.72	141.81	133.67	138.67
$L1D_{Total}$ (mT)	491.87	475.51	464.16	608.84	589.25	581.13
The predicted broken wire numbers	4 (3.59)	4 (3.47)	4 (3.30)	5 (4.29)	5 (4.41)	5 (4.19)

were conducted for cases with 2–5 broken wires, each with a width of 10 mm, under varying distributions, as illustrated in Fig. 20. Distributions 1, 2, and 3 were characterized by broken wires separated by 1, 2, and 3 intact wires, respectively, reflecting a gradual increase in broken-wire discreteness.

The accuracy of the proposed method in quantifying the number of broken wires across different distributions was evaluated based on the simulation data. The defects, comprising different combinations of numbers and distributions, were labeled as Defects 1# to 12#. The quantification results are presented in Tables 2 and 3. The maximum prediction error for defect width was 14.7 %, while the minimum error was 0.8 %. The predicted number of broken wires corresponded exactly to the preset values across all distributions. However, the prediction accuracy for the widths of dispersed defects was lower than that for continuously distributed defects. This reduction in accuracy occurs because the training data were based on continuously distributed broken-wire patterns, limiting generalizability to discrete distributions. Variations in distribution do not affect the accuracy of quantifying the number of broken wires. Thus, the proposed method consistently enabled accurate quantification of the number of broken wires, confirming its robustness under diverse conditions.

4.2. Method verification by experiment

4.2.1. Experimental setup

The simulations verified that the proposed method accurately predicts the number of broken wires for defects with different widths and distribution patterns. Experimental testing was performed using a cable specimen to validate these findings.

The multilayer-arranged Hall element (MAHE) sensor developed in a previous study was employed to capture the MFL signals generated by broken wires [23]. Fig. 21 (a) exhibits that the customized MAHE sensor was designed for cables of the PES7-127 specification, consisting of 127 steel wires with individual diameters of 7 mm and an overall outer diameter of 109 mm. The sensor was fabricated with an inner diameter of 111 mm to account for maximal manufacturing tolerances of ±2 mm. Structurally, the sensor integrates six identical MAHE sensor PCBs, as shown in Fig. 21 (b), with each PCB containing 10 Hall element groups arranged circumferentially around the cable. Each Hall element group incorporates four radially distributed Hall elements, enabling a single MAHE sensor PCB to achieve sensing coverage over a 60° arc of the cable. Each Hall element used in this study was an Allegro A1302 linear

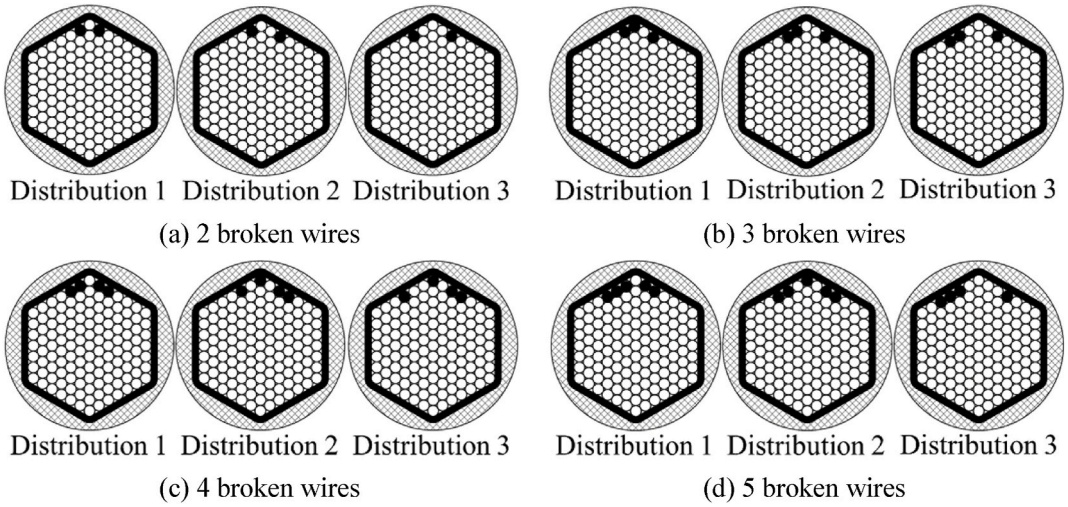

Fig. 20. Distributions of the broken wires with different numbers.

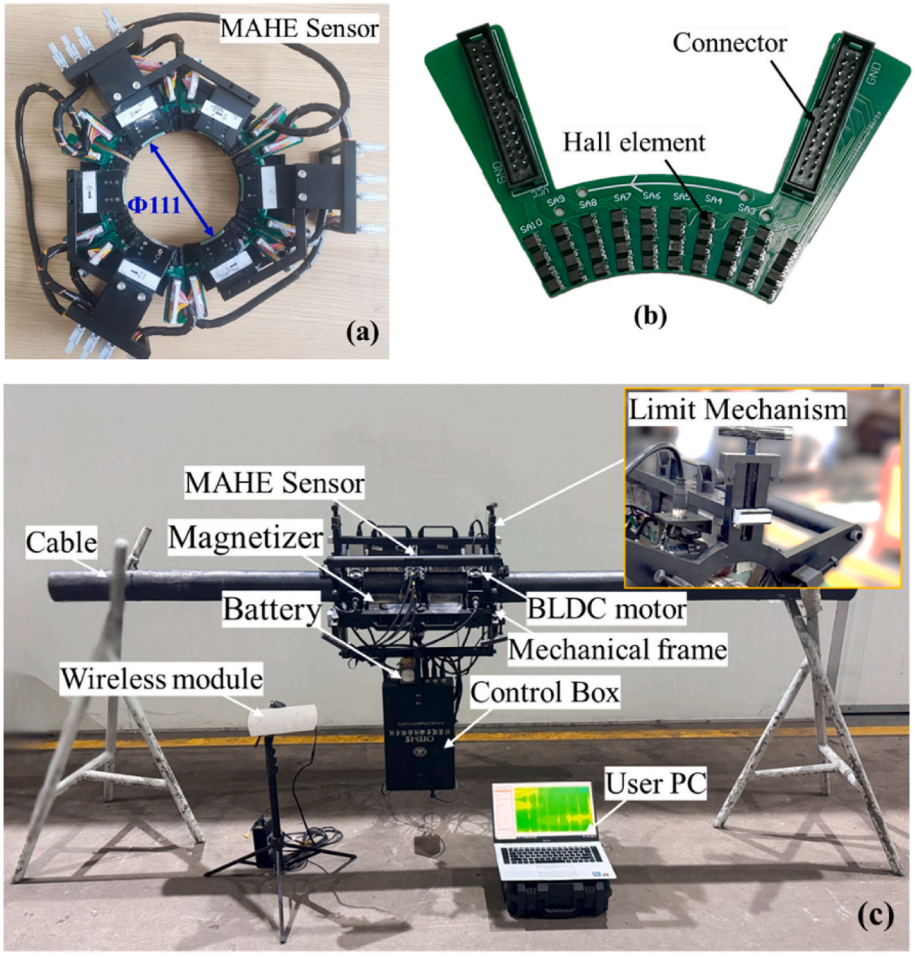

Fig. 21. (a) Photograph of the MAHE sensor. (b) PCB board of the sensor. (c) Photograph of the experimental system.

Hall-effect sensor. Due to its high sensitivity (13 mV/mT), broad linear range (±0.1 T), and low noise floor (150 μV rms), this sensor effectively captures weak MFL signals [43]. Its compact SIP-3 package (4.00 × 3.00 × 1.50 mm) further allows the high-density Hall element configuration required for circumferential group layouts on each PCB. These features collectively ensure the reliable acquisition of 3D spatial MFL data during practical testing. Signal outputs were routed through bilateral PCB-mounted connectors, ensuring synchronous data acquisition across all measurement nodes. An experimental system for bridge cable testing was constructed using this sensor.

Fig. 21 (c) indicates that the experimental system comprises two primary components: the testing robot and the user PC. The robot consists of a mechanical frame, the MAHE sensor, a magnetizer, a BLDC motor, a control box, and a battery. The magnetizer dimensions are consistent with those used in the simulation model shown in Fig. 4. It was constructed using N52 permanent magnets (Shenzhen Xun Zhi Ci Technology Co., Ltd.) with a remanence of 1.438 T and an intrinsic coercivity of 941,000 A/m. FEM simulations confirmed that this configuration provided a magnetic flux density exceeding 1.7 T within the cable sample, ensuring complete saturation. The MAHE sensor then captured the resulting MFL signals. The mechanical structure connected all components, with a limiting mechanism designed to press the probe tightly against the cable, minimizing lift-off fluctuations between the magnetizer, the sensor, and the cable during movement. The control box integrated modules for motor control, data acquisition, and wireless transmission. The motor control module, developed using the ROBOMASTER development board, drove the BLDC motor (model: ROBOMASTER M3508, with a no-load speed of 482 RPM and a continuous maximum torque of 3 N•m) to move the robot at controlled speeds ranging from 4 to 12 m/min. The data acquisition module, developed based on the AD7606 and ADG706 chips, supported up to 512 channels for effective data sampling at 1 KSPS, which satisfied the requirements for acquiring signals from the MAHE sensor [44]. Wireless transmission was achieved using an industrial-grade wireless bridge, enabling stable data transfer over distances of at least 1 km. Therefore, the robot successfully acquired MFL signals in 3D space at a speed of 4 m/min with a 1 mm sampling interval and transmitted the captured data to the remote user PC in real time. The entire testing robot was powered by a 24 V battery.

4.2.2. *Quantification experiment*

The cable specimen employed was of PES7-127 specification, with an outer diameter of 109 mm and a total length of 2800 mm. A 10 mm-wide single broken wire was incorporated into the first layer of the cable, and the detected MFL signal was utilized as the reference signal to calculate LID values corresponding to single broken wires of varying widths, based on Eq. (17). Fig. 22 illustrates the four array slices of the MFL signal derived from this broken wire. These slices exhibit a high degree of similarity to the corresponding slices of the simulated signal presented in Fig. 6. The acquired MFL signals were initially recorded in millivolts (mV) as raw voltage outputs from the A1302 Hall sensors. For consistency with the simulated data (in mT) and to enable quantitative analysis, all raw signals were converted to magnetic flux density (mT) using the sensor's 13 mV/mT sensitivity coefficient prior to storage, ensuring that experimental data were stored in mT for subsequent analysis. Both similarity and mean square error (MSE) were calculated

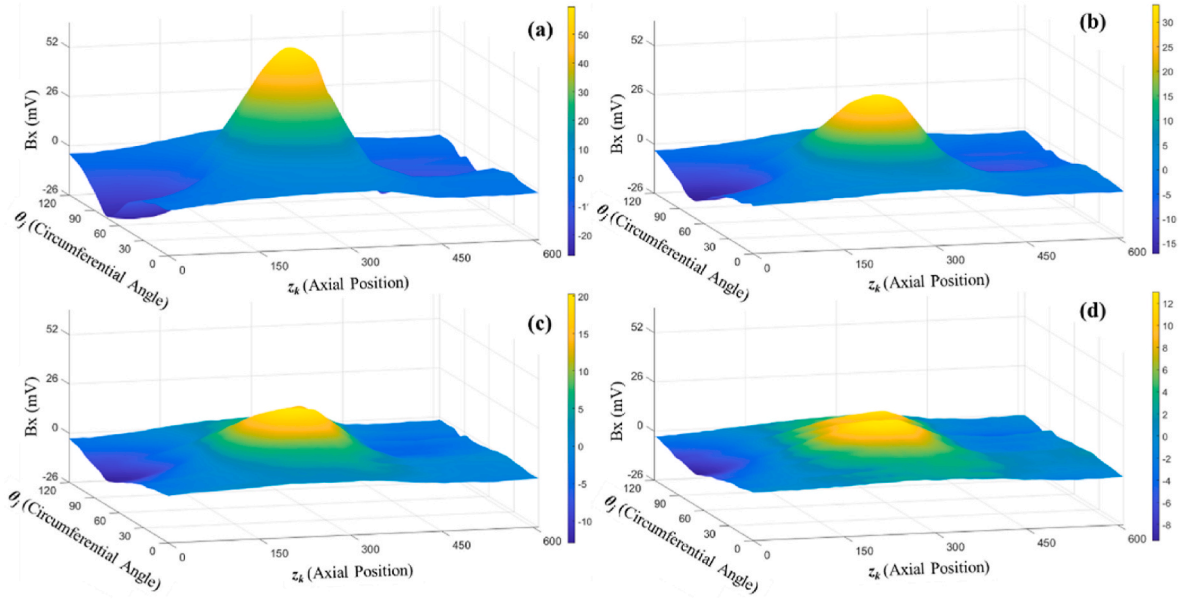

Fig. 22. Array slices $\boldsymbol{B_{MFL}}$ (1, :,) to $\boldsymbol{B_{MFL}}$ (4, :,) of the MFL signal of the single broken wire.

between the corresponding slices from the simulated signal and the experimental signal. The similarity values for the four slice pairs were 0.974, 0.986, 0.991, and 0.995, respectively, with corresponding MSE values of 0.581, 0.208, 0.0955, and 0.051. Accordingly, due to the high similarity and low MSE, the inversion model constructed using simulated data can be directly applied to quantify actual broken wires in bridge cables.

A cable specimen containing 8 clusters of broken wires was fabricated in accordance with the schematic diagram shown in Fig. 23 to validate the method's capability to quantitatively evaluate broken wires with varying numbers and distributions in engineering applications. Each cluster of broken wires has a width of 10 mm, with a spacing of 200 mm between adjacent defects, and they are arranged along the axial direction of the cable. The numbers and distributions of each defect are presented in Fig. 23 (b).

In this study, rather than relying only on steel wire bundles for experimentation, cable specimens featuring multiple clusters of broken wires were fabricated through a complete cable manufacturing process, better replicating real-world engineering conditions. Fig. 24 illustrates the fabrication process of the cable specimen. Fig. 24 (a) depicts the fabrication of a single broken wire: two 7 mm-diameter steel wires were joined using a plastic sleeve, with a 10 mm-wide solid plastic filler embedded in the middle of the sleeve. The arrangement of broken wires strictly followed the distribution and numerical specifications outlined in Fig. 23. Then, these steel wires with broken wire defects were secured together with other intact wires to form a 127-wire bundle, which was then wrapped and fixed into a regular hexagonal structure, as shown in Fig. 24 (b). Fig. 24 (c) reveals that the cable specimen was completed after the wire bundle underwent the extrusion process.

The fabricated cable exhibited a curved shape, which resulted from the inherent curvature of the raw steel wires. This condition introduced two potential issues: first, broken wires can shift during wrapping and extrusion, leading to deviations from the intended 10 mm width with specific errors; second, the fracture surfaces of multiple broken wires at each location can be non-parallel, with slight misalignment. Although these conditions made the experimental specimens less than ideal, they

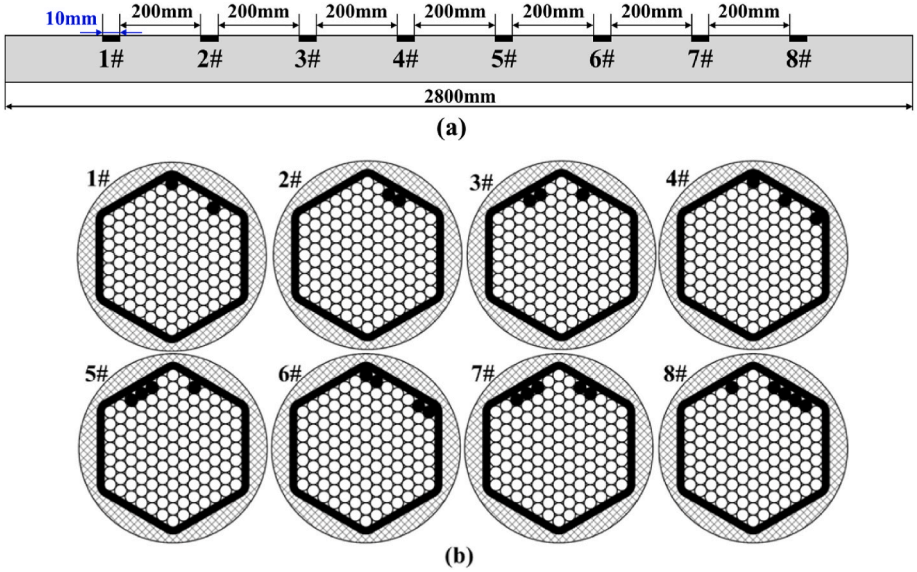

Fig. 23. Schematic diagram of broken wires positions in the cable specimen.

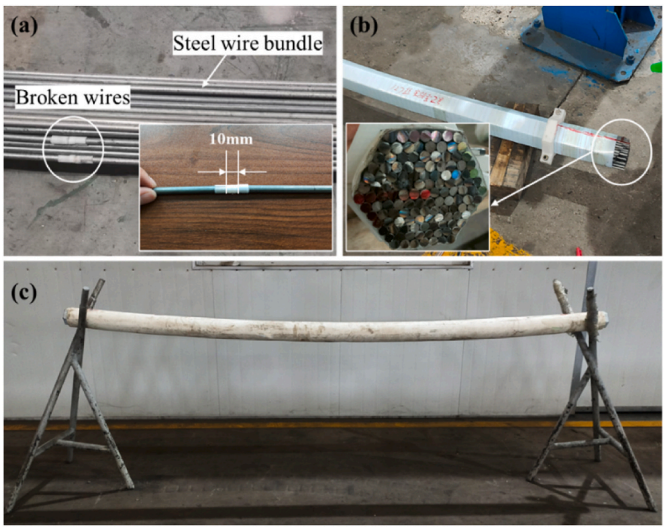

Fig. 24. The manufacturing process of the cable specimen.

reflected engineering reality, where defects such as broken wires in actual scenarios are inherently random in distribution and width. In addition, the focus of this study lies in the quantification of broken wire numbers, and the mentioned issues primarily affected the distribution and width of broken wires without altering the initially set number of broken wires.

This cable specimen was tested using the experimental system shown in Fig. 21 (c). The cable was positioned horizontally on the support, and the robot traveled axially along the cable to collect MFL signals, with five repeated scans performed. All defect signals were extracted, with a circumferential extraction angle of 120° (corresponding to 20 circumferential channels) and an axial extraction length of 60 mm. The MFL signal array with dimension sizes of 4 × 120 × 600 was constructed through circumferential and axial interpolation. Figs. 25 and 26 present the array slices of the MFL signal of Defects 3# and 4#, respectively. Although both defects contained three broken wires, their signal waveform morphologies differed due to variations in the distribution of broken wires.

Experimental quantification results obtained using the proposed method are presented in Table 4. The detailed findings are as follows:

(a) For the 1# and 2# defects with an actual number of two broken wires: all five quantification results for 1# are accurate, each identifying two broken wires. For 2#, four out of five quantifications are correct, while one overestimates the number as three.
(b) For the 3# and 4# defects with an actual number of three broken wires: four out of five quantifications for 3# are accurate, with one overestimating the number as four. All quantifications for 4# are correct, each indicating three broken wires.
(c) For the 5# and 6# defects with an actual number of four broken wires: all five quantifications for both defects accurately indicate four broken wires.
(d) For the 7# and 8# defects with an actual number of five broken wires: only one quantification is accurate for each defect. The remaining four quantifications for 7# overestimate the number as six, whereas those for #8 underestimate it as three.

The results demonstrate that quantification accuracy is higher for defects with ≤4 broken wires. In practical engineering, quantification errors within one wire are generally acceptable for load-bearing components such as steel wire ropes [45]. With a tolerance of ±1 error, the accuracy for defects with ≤4 broken wires reach 100 %. However, for this cable specification, replacement is required when the number of broken wires reaches three or more. Since all predictions for the preset five-broken-wire defects were ≥3, the proposed method remains effective for ensuring safety.

5. Conclusion

This study proposes a novel quantitative evaluation method for broken wires in bridge cables based on MFL signals, and the key findings and contributions are summarized as follows:

First, a four-step method is introduced to quantify the number of broken wires: (a) capturing the 3D spatial magnetic leakage field; (b) extracting two types of features, namely the global feature L1D and local features (multi-scale waveform feature array), which are applied to predict the number and width of broken wires, respectively; (c) compressing the feature array via MPCA to preserve essential information, followed by defect width prediction using the ENCR model; and (d) using the superposition property of L1D, whereby the number of broken

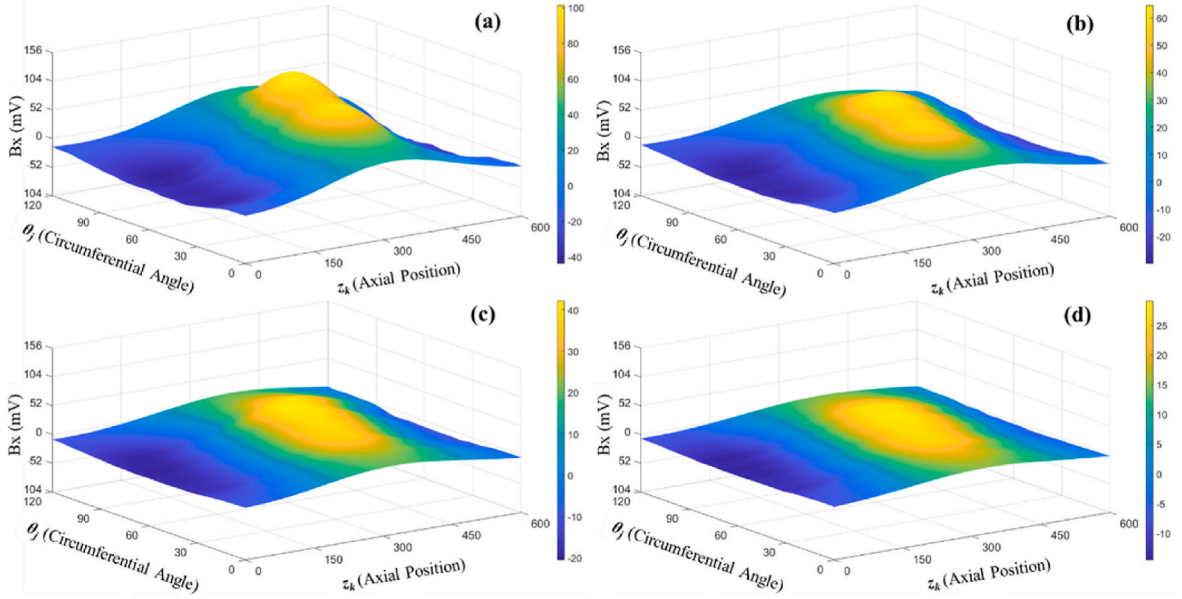

Fig. 25. Array slices $\boldsymbol{B}_{MFL}(1, :,)$ to $\boldsymbol{B}_{MFL}(4, :,)$ of the MFL signal of 3# defect.

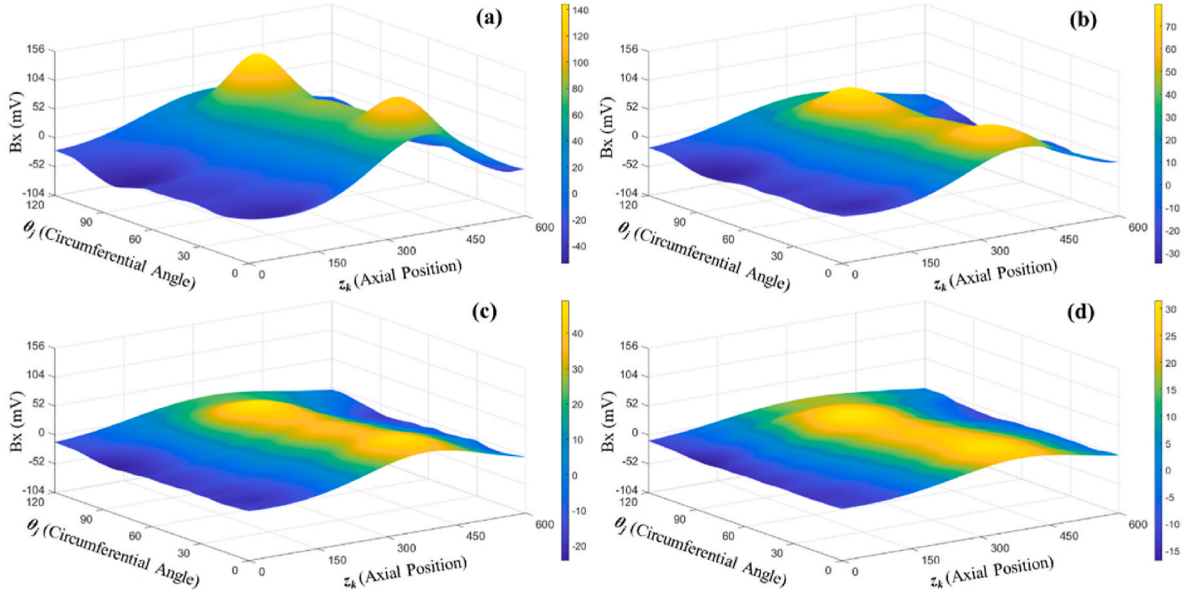

Fig. 26. Array slices $\boldsymbol{B_{MFL}}(1, :,)$ to $\boldsymbol{B_{MFL}}(4, :,)$ of the MFL signal of 4# defect.

Table 4
Quantification results of the experiment.

Defect	Preset number	Quantification results				
		Scan 1	Scan 2	Scan 3	Scan 4	Scan 5
1#	2	2	2	2	2	2
2#	2	2	2	2	2	**3**
3#	3	3	3	3	3	**4**
4#	3	3	3	3	3	3
5#	4	4	4	4	4	4
6#	4	4	4	4	4	4
7#	5	5	**6**	**6**	**6**	**6**
8#	5	5	**3**	**3**	**3**	**3**

wires is calculated as the ratio of the total L1D ($L1D_{Total}$) to the L1D corresponding to a single wire ($L1D_{Single}$) at the predicted width.

Second, FEM simulations are employed to determine the optimal dimension sizes of both MFL signals and feature arrays. MFL signals with optimized dimensions demonstrate that, for a given defect width, the L1D calculated from MFL signals satisfies linear superposition with respect to the number of broken wires. This linear relationship, with goodness-of-fit values exceeding 0.999, enables proportional quantification through linear superposition. In addition, each element in the feature arrays with optimized parameters effectively reflects variations in the width of broken wires, supporting accurate width prediction as a critical intermediate variable.

Third, the proposed method is validated through both simulation and experiment. This performance is achieved with a small training dataset of only 30 samples. Simulation results reveal that the width prediction error ranges from 0.78 % to 14.7 % under different distributions of broken wires. The method achieves 100 % accuracy in counting broken wires across various widths and distributions, utilizing accurate width prediction results as an intermediate variable. Experimental validation on a PES7-127 cable specimen confirms 100 % quantification accuracy for defects with $\leq$4 broken wires, within an error tolerance of $\pm$1 wire, verifying its applicability for engineering safety assessments.

Future work focuses on three key directions: (1) improving quantification accuracy in scenarios involving a larger number of broken wires in practical bridge cable applications; (2) exploring quantitative evaluation methods for corrosion damage and internal broken wires using 3D spatially sampled MFL signals; and (3) extending the research to partial wire breaks, since the current study concentrates exclusively on complete breaks. This extension includes categorizing the typical morphologies of partial breaks, establishing correlations between their morphological features and 3D MFL signal responses through parametric simulations, and optimizing the quantitative algorithm to adapt to the diverse morphologies of partial fractures.

CRediT authorship contribution statement

Lingsi Sun: Writing – original draft, Validation, Methodology, Investigation, Formal analysis, Conceptualization. **Wenlong Zhang:** Writing – review & editing, Validation, Methodology. **Huanze Liu:** Validation. **Runyu Wang:** Software, Data curation. **Shuyu Duan:** Writing – review & editing. **Lijun Jiang:** Validation. **Xinjun Wu:** Writing – review & editing, Supervision, Project administration, Funding acquisition.

Declaration of competing interest

The authors declare that they have no known competing financial interests or personal relationships that could have appeared to influence the work reported in this paper.

Acknowledgments

This work was supported by the National Natural Science Foundation of China (Grant No. U21A20139). The authors also acknowledge Zhiwei Tao for experimental preparation, Ziye Wang for methodological discussion, and Dr. Yiqing Zou for technical assistance during experimentation.

Data availability

Data will be made available on request.

References

[1] Ding Y, Ye X-W, Su Y-H, Zheng X-L. A framework of cable wire failure mode deduction based on bayesian network. Structures 2023;57:104996. https://doi.org/10.1016/j.istruc.2023.104996.
[2] Tochaei EN, Fang Z, Taylor T, Babanajad S, Ansari F. Structural monitoring and remaining fatigue life estimation of typical welded crack details in the manhattan bridge. Eng Struct 2021;231:111760. https://doi.org/10.1016/j.engstruct.2020.111760.

[3] Ren W-X, Blandford GE, Harik IE. Roebling suspension bridge. I: finite-element model and free vibration response. J Bridge Eng 2004;9:110–8. https://doi.org/10.1061/(ASCE)1084-0702(2004)9:2(110).

[4] Drissi Habti M, Yanev B, Betti R. Suspension bridge cables: pathologies, inspection, alternative materials. Mater Eval 2009;67.

[5] Huang X, Li S. Economic and industrial development SignificantlyContribute to acidity and ionic compositions of rainwaterin China. Water 2024;16:193. https://doi.org/10.3390/w16020193.

[6] Guowen Y, Shicong Y, Jinquan Z, Yanling L. Analysis of corrosion-fatigue damage and fracture mechanism of in-service bridge cables/hangers. Adv Civ Eng 2021;2021:6633706. https://doi.org/10.1155/2021/6633706.

[7] Xia R, Zhang H, Jiang L, Tao Q, Zhang S, Zhou J. Circumferential multi-point corrosion status assessment of steel cables considering self-magnetic flux leakage superposition effect. Constr Build Mater 2024;449:138315. https://doi.org/10.1016/j.conbuildmat.2024.138315.

[8] Ali K, Katsuchi H, Yamada H. Comparative study on structural redundancy of cable-stayed and extra dosed bridges through safety assessment of their stay cables. Eng Times 2021;7:111–23. https://doi.org/10.1016/j.eng.2020.07.021.

[9] Meng YJ, Zhou XY. Research on long-span old bridge's dynamic reliability under vehicular load. Adv Mater Res 2011;295–297:2161–70. https://doi.org/10.4028/www.scientific.net/AMR.295-297.2161.

[10] Jiang L, Zhang H, Xia R, Zhou J, Liu S, Ding Y. Research on identification method of cable cross-sectional loss rates based on multiple magnetic characteristic indicators. J Nondestruct Eval 2024;43:64. https://doi.org/10.1007/s10921-024-01079-4.

[11] Ministry of Housing and Urban - Rural Development of the People's Republic of China. Technical standard of maintenance for city bridge. 2018. CJJ 99 - 2017).

[12] Zhang H, Li H, Zhou J, Tong K, Xia R. A multi-dimensional evaluation of wire breakage in bridge cable based on self-magnetic flux leakage signals. J Magn Magn Mater 2023;566:170321. https://doi.org/10.1016/j.jmmm.2022.170321.

[13] Kong X, Liu Z, Liu H, Hu J, Deng L. Recent advances on inspection, monitoring, and assessment of bridge cables. Autom ConStruct 2024;168:105767. https://doi.org/10.1016/j.autcon.2024.105767.

[14] Li G, Zhao Z, Li Y, Li C-Y, Lee C-C. Preprocessing acoustic emission signal of broken wires in bridge cables. Appl Sci 2022;12:6727. https://doi.org/10.3390/app12136727.

[15] Zhao S, Li G, Wang C. Bridge cable damage identification based on acoustic emission technology: a comprehensive review. Measurement 2024;237:115195. https://doi.org/10.1016/j.measurement.2024.115195.

[16] Duan S, Wu X, Zou Y, Jiang L. Corrosion characterization of steel wires based on persistent homology theory for magnetostrictive guided wave testing signal. Struct Health Monit 2023;22:2147–65. https://doi.org/10.1177/14759217221119790.

[17] Antipov AG, Markov AA. 3D simulation and experiment on high speed rail MFL inspection. NDT E Int 2018;98:177–85. https://doi.org/10.1016/j.ndteint.2018.04.011.

[18] Zhang D, Zhang E, Yan X. Quantitative method for detecting internal and surface defects in wire rope. NDT E Int 2021;119:102405. https://doi.org/10.1016/j.ndteint.2021.102405.

[19] Wang R, Chen Y, Yu H, Xu Z, Tang J, Feng B, et al. Defect classification and quantification method based on AC magnetic flux leakage time domain signal characteristics. NDT Int 2025;149:103250. https://doi.org/10.1016/j.ndteint.2024.103250.

[20] Ding D, Lu J, Xu F. Designing and investigating a nondestructive magnetic flux leakage detection system for quantitatively identifying wire defects. IEEE Sens J 2022;22:20360–72. https://doi.org/10.1109/JSEN.2022.3206325.

[21] Abdelsalam E, Kafiah F, Kiswani S, Ibrahim D, Ghorbanpoor A. MFL based prototype and experimental work for detection of defects in cables of bridge structures. JORDAN JOURNAL OF MECHANICAL AND INDUSTRIAL ENGINEERING 2020;14:361–70.

[22] Liu X, Xiao J, Wu B, He C. A novel sensor to measure the biased pulse magnetic response in steel stay cable for the detection of surface and internal flaws. Sens Actuators, A 2018;269:218–26. https://doi.org/10.1016/j.sna.2017.11.005.

[23] Sun L, Wang J, Tao Z, Duan S, Wu X. A sensor based on multilayer-arranged hall elements for MFL detection of broken wires in bridge cables. Sensor Actuator Phys 2025;391:116668. https://doi.org/10.1016/j.sna.2025.116668.

[24] Yuan Y, Liu X, Pu G, Wang T, Zheng D. Temporal and spatial variability of corrosion of high-strength steel wires within a bridge stay cable. Constr Build Mater 2021;308:125108. https://doi.org/10.1016/j.conbuildmat.2021.125108.

[25] Wen-cheng XU, Shi-qian YAO, Xu XIE, Xiang-long ZHENG. Research on service performance and replacement condition of rusty steel cable. Res Serv Perform Replace Cond Rusty Steel Cable 2021;66:133–9.

[26] Liu S, Chen M. Wire rope defect recognition method based on MFL signal analysis and 1D-CNNs. Sens 2023;23:3366. https://doi.org/10.3390/s23073366.

[27] Li Y, Sun C, Liu Y. Magnetic flux leakage testing method for pipelines with stress corrosion defects based on improved kernel extreme learning machine. Electronics 2023;12:3707. https://doi.org/10.3390/electronics12173707.

[28] He H, Tan Y, Zhang W. A wavelet tensor fuzzy clustering scheme for multi-sensor human activity recognition. Eng Appl Artif Intell 2018;70:109–22. https://doi.org/10.1016/j.engappai.2018.01.004.

[29] Thaker P, Mohan BR. Enhancing deep compression of CNNs: a novel regularization loss and the impact of distance metrics. IEEE Access 2024;12:172537–47. https://doi.org/10.1109/access.2024.3498901.

[30] Sun L, Wu X, Ouyang Q, Wang J. A novel broken wire evaluation method for bridge cable magnetic flux leakage testing under lift-off uncertainty. J Magn Magn Mater 2023;570:170525. https://doi.org/10.1016/j.jmmm.2023.170525.

[31] Zhang K, Zhang X, Zhang Z. Tucker tensor decomposition on FPGA. 2019 IEEE/ACM international conference on computer-aided design (ICCAD). Westminster, CO, USA: IEEE; 2019. p. 1–8. https://doi.org/10.1109/ICCAD45719.2019.8942103.

[32] Du X, Groening L. Compression and noise reduction of field maps. Phys Rev Accel Beams 2018;21:84601. https://doi.org/10.1103/PhysRevAccelBeams.21.084601.

[33] Xuan W, Chen P, Li R, Wang F, Fu K, Wen Z. A targeted one dimensional fully convolutional autoencoder network for intelligent compression of magnetic flux leakage data. Sci Rep 2025;15:11455. https://doi.org/10.1038/s41598-025-96282-2.

[34] Al Mamun A, Islam MI, Shohag MAS, Al-Kouz W, Noor KA. Multilinear principal component analysis-based tensor decomposition for fabric weave pattern recognition from high-dimensional streaming data. Pattern Anal Appl 2024;27. https://doi.org/10.1007/s10044-024-01318-4.

[35] Andahmou A. MPCA and MDA via einstein product. Comput Appl Math 2024;43. https://doi.org/10.1007/s40314-024-02866-5.

[36] Billio M, Casarin R, Iacopini M, Kaufmann S. Bayesian dynamic tensor regression. J Bus Econ Stat 2023;41:429–39. https://doi.org/10.1080/07350015.2022.2032721.

[37] Peng J, Lin H, Lian H. Tensor train regression with convex regularization. Statistics 2025:1–22. https://doi.org/10.1080/02331888.2025.2482070.

[38] Chen X, Sun Z-L, Zhang Y. 3D shape reconstruction with a multiple-constraint estimation approach. Front Neurosci 2023;17. https://doi.org/10.3389/fnins.2023.1191574.

[39] Liu H, Yang L, Zhang L, Shang F, Liu Y, Wang L. Accelerated stochastic variance reduction gradient algorithms for robust subspace clustering. Sens 2024;24:3659. https://doi.org/10.3390/s24113659.

[40] Tao Z, Sun L, Wu X. Design of magnetic flux leakage detection magnetizer for broken wire in bridge cable. Instrum Tech Sens 2025:28–33.

[41] Ningxiang Y, Xiucheng L, Yinghong C, Junwu X. Circular sensor array for surface flaws detection in stay cable based on magnetic flux leakage. 2019.

[42] Zhong XY, Zhang XH. Research of non-destructive testing of wire rope using magnetic flux leakage. Appl Mech Mater 2012;189:255–9. https://doi.org/10.4028/www.scientific.net/amm.189.255.

[43] MicroSystems Allegro. Continuous-time Ratiometric linear Hall-effect sensor ICs. Allegro MicroSystems; 2020.

[44] Sun L, Tao Z, Ouyang Q, Wu X. Development of multi-channel magnetic flux leakage testing system for bridge cables. E-J Nondestruct Test 2024;29. https://doi.org/10.58286/29932.

[45] Gu W, Chu J. Characteristic values analysis and fuzzy discernment for the fault status of the wire rope. Chin J Mech Eng 2002;38:122–5.